List of Publications

This thesis is based on the work contained in following papers:

- **The role of the anions in concentrated electrolytes for lithium-sulfur batteries**
  Aginmariya Kottarathil, Zaher Slim, Hafiz Ahmad Ishfaq, Steffen Jeschke, Grażyna Zofia Żukowska, Maciej Marczewski, Katarzyna Lech, Patrik Johansson and Wladyslaw Wieczorek.
  Contribution: I performed the experiments, data analysis and took the lead in manuscript preparation and discussion with co-authors.
  Accepted

- **Hückel anion based concentrated electrolytes for lithium-sulfur batteries**
  Aginmariya Kottarathil, Zaher Slim, Tomooki Hosaka, Steffen Jeschke, N.Tan Luong, Grażyna Zofia Żukowska, Maciej Marczewski, Patrik Johansson and Wladyslaw Wieczorek.
  Manuscript
  Contribution: I performed the experiments, computational work, data analysis and took the lead in manuscript preparation and discussion with co-authors.

- **Insights to polysulfide dissolution and diffusion by *operando* Raman spectroscopy**
  N.Tan Luong, Aginmariya Kottarathil, Wladyslaw Wieczorek and Patrik Johansson.
  Manuscript
  Contribution: I participated in the experiments, data analysis and contributed in manuscript preparation and discussion with co-authors.

- **There is Plenty of Room in the Compositional Space: The Impact of New Battery Electrolyte Concepts**
  Maciej Marczewski, Maciej Dranka, Aginmariya Kottarathil, Martin Karlsmo, Kasper Westman, Mirna Alhanash, Carolina Cruz, Johanna Timhagen, Tomooki Hosaka, N.Tan Luong, Zaher Slim, Clément Pechberty, Alexandre Ponrouch, Deyana Tchitchekova, Sara Drvarič Talian, , Hafiz Ahmad Ishfaq, Matea Raić, Tjaša Pavčnik, Jan Bitenc, Władysław Wieczorek and Patrik Johansson.
  Manuscript
  Contribution: I contributed to the prospects of concentrated electrolytes for lithium-sulfur batteries part of the review article.

Acknowledgements

I am extremely grateful to my supervisors: Prof. Wladyslaw Wieczorek for giving me the opportunity, support, and encouragement throughout my PhD journey at Warsaw University of Technology, and Prof. Patrik Johansson for hosting me at Chalmers, and for providing insightful feedback, patience, and constant guidance.

I want to acknowledge the financial support from the DESTINY PhD programme (European Union's Horizon 2020 research and innovation programme under the Marie Skłodowska-Curie Actions COFUND Grant Agreement No. 945357) for funding my PhD studies. A big thank you to Prof. Christian Masquelier, Miss Louise Vrand, and Miss Béatrice Messana for making my DESTINY PhD journey possible and wonderful.

I would like to express special thanks to: Dr Maciej Marczewski for supporting me at WUT with administrative tasks and for helpful discussions, Prof. Grazyna Zukowska for all the Raman spectroscopy discussions, Maciej Smolinski for the preparation of cathodes used in this work, Dr Marek Broszkiewicz and Claudia for helping with the EIS and cryostat. I extend my gratitude to Dr Ezio Zhangellini for his initial help at Chalmers, for assistance with different equipments, and for valuable life lessons. Thank you, Dr Patricia Huijbers, for the feedback and your support. Dr Zaher Slim and Dr Tomooki Hosaka for draft corrections and engaging meetings, Dr Tan Luong for helping with *operando* Raman spectroscopy and discussions. Dr Soniya Rao for introducing me to computational chemistry and Dr Steffen Jeschke for guidance and support in COSMO-RS and machine learning. Dr Carolina Cruz for helping me to resolve LaTeX questions, Ahmad Ishfaq and Matteo Palluzzi for supporting me in the lab and helping with Origin software.

A big thanks to other colleagues at WUT and Chalmers for their support. I am also thankful to some of my friends: Aleena, Brigette, Dimitra, Elosa, Femi, Juhi, Nati, Nidhin, Shreya and Sona – your availability means a lot.

I am indebted to my family for their unconditional love and understanding. Thank you, Papa, for believing in me and allowing me to pursue my dreams despite societal norms. Thanks to my younger sisters, Anju, Aleena, and Ann for their constant care and mentorship. My heartfelt thanks to Anjali Aunty, Sherly Aunty, and Uncle John for supporting me, especially during my school years.

I dedicate this to you: Grandpa, Grandma and Mom.

Abstract

Lithium-sulfur (Li-S) batteries have a great potential to be the next-generation batteries and meet the rapidly increasing demand for electric and hybrid vehicles. In principle, Li-S batteries, with their high energy density, low cost and environmental friendliness, can complement commercial lithium-ion batteries. However, the practical application of these Li-S batteries is hindered by short cycle life and capacity fading which is primarily caused by polysulfide (PS) dissolution and shuttling in the electrolyte. One promising approach to mitigate PS dissolution is by increasing the salt concentration in the electrolyte using highly concentrated electrolytes. This thesis presents a comprehensive study on the influence of different salts in concentrated electrolytes for Li-S batteries.

We systematically examine the role of anions in lithium salts, focusing on conventional LiTFSI, LiTf, and the Huckel salt LiTDI in DOL:DME solvent mixture up to maximum salt solubility. At high salt concentrations, the high amount of ion-pairs and aggregates and low amount of free solvent reduces the PS solubility and enhances Li-S battery performance. Due to the superior electrochemical performance of the LiTDI-based electrolytes at comparable concentrations with LiTFSI and LiTf, we further explore other Huckel salts, specifically LiPDI and LiHDI, which differ in perfluoro chain length. These Huckel anion-based electrolytes exhibited Li-S battery capacity similar to each other. Furthermore, the addition of $LiNO_3$ additive in the electrolytes enhances the coulombic efficiency.

To gain a better understanding of PS solubility and diffusion in various concentrated electrolytes, we employ *in situ / operando* Raman spectroscopy and advanced modelling efforts using a supervised machine learning approach. For the latter, we combine a conductor-like screening model with a multiple linear regression model to effectively predict polysulfide solubility across different electrolyte compositions.

Keywords: Li-S batteries, highly concentrated electrolytes, Hückel-anions, FTIR, Raman, *in situ / operando*, COSMO-RS, machine learning

Streszczenie

Baterie litowo-siarkowe (Li-S) mają ogromny potencjał, aby stać się bateriami nowej generacji i sprostać szybko rosnącemu zapotrzebowaniu na pojazdy elektryczne i hybrydowe. Zasadniczo baterie Li-S, dzięki swojej wysokiej gęstości energii, niskim kosztom i przyjazności dla środowiska, mogą uzupełniać komercyjne baterie litowo-jonowe. Jednak praktyczne zastosowanie tych baterii Li-S jest utrudnione przez krótki cykl życia i zanikanie pojemności, co jest głównie spowodowane rozpuszczaniem i migracją polisiarczków (PS) w elektrolicie. Jednym z obiecujących podejść do złagodzenia problemu rozpuszczania PS jest zwiększenie stężenia soli w elektrolicie za pomocą wysoko stężonych elektrolitów. Niniejsza praca przedstawia kompleksowe badanie wpływu różnych soli w stężonych elektrolitach dla baterii Li-S.

Systematycznie badamy rolę anionów w solach litu, koncentrując się na konwencjonalnych LiTFSI, LiTf oraz soli Huckla LiTDI w mieszaninie rozpuszczalników DOL:DME aż do maksymalnej rozpuszczalności soli. Przy wysokich stężeniach soli, wysoka ilość par jonowych i agregatów oraz niska ilość wolnego rozpuszczalnika zmniejsza rozpuszczalność PS i poprawia wydajność baterii Li-S. Ze względu na doskonałą wydajność elektrochemiczną elektrolitów opartych na LiTDI przy porównywalnych stężeniach z LiTFSI i LiTf, dalej badamy inne sole Huckla, w szczególności LiPDI i LiHDI, które różnią się długością łańcucha perfluorowego. Te elektrolity na bazie anionów Huckla wykazały podobną pojemność baterii Li-S. Ponadto dodatek $LiNO_3$ do elektrolitów zwiększa sprawność kolumbowską.

Aby lepiej zrozumieć rozpuszczalność i dyfuzję PS w różnych stężonych elektrolitach, stosujemy spektroskopię Ramana *in situ / operando* oraz zaawansowane modelowanie z wykorzystaniem podejścia uczenia maszynowego. W tym celu łączymy model przesiewania przewodnika z modelem regresji wieloliniowej, aby skutecznie przewidywać rozpuszczalność polisiarczków w różnych kompozycjach elektrolitów.

Słowa kluczowe: baterie Li-S, wysoko stężone elektrolity, aniony Huckla, FTIR, Raman, *in situ / operando*, COSMO-RS, uczenie maszynowe

List of abbreviations

AGG	Aggregates
CIP	Contact ion-pair
COSMO-RS	Conductor-like screening model for real-solvents
DAD	Diode array detector
DFT	Density functional theory
DME	1,2 dimethoxyethane
DN	Donor number
DOL	Dixoloane
EIS	Electrochemical impedance spectroscopy
ESW	Electrochemical stability window
EV	Electric vehicles
FTIR	Fourier transform infrared
HCEs	Highly concentrated electrolytes
HPLC	High-performance liquid chromatography
LIB	Lithium-ion batteries
LiHDI	Lithium 4,5 dicyano-2-(heptafluoropropyl)imidazole
LiPDI	Lithium 4,5 dicyano-2-(pentafluoroethyl)imidazole
LiPSs	Lithium polysulfides
Li-S	Lithium-sulfur batteries
LiTDI	Lithium 4,5 dicyano-2-(trifluoromethyl)imidazole
LiTf	Lithium trifluoromethanesulfonate
LiTFSI	Lithium bis(trifluoromethanesulfonyl)imide
MD	Molecular dynamics
ML	Machine learning
MLR	Multiple linear regression
OCV	Open circuit voltage
OLS	Ordinary least squares
PS	Polysulfide
PSs	Polysulfides
QSAR	Quantitative structure activity relationship
QSPR	Quantitative structure property relationship
SEI	Solid electrolyte interphase
SSIP	Solvent-separated ion-pair

List of symbols

A	Cross-sectional area
a	Real part on the x-axis
$A_{n,\max}$	Peak absorbance of the n-th Gaussian component centered at wavenumber v_n
$A(v)$	Absorbance at a specific wavenumber v
b	Imaginary part on the y-axis
c	Speed of light
°C	Degree Celsius
D_i	Diffusion constant of a polysulfide species i
E_1	Energy at ground level
h	Planck constant
i	Imaginary unit
k_B	Boltzmann constant
K_{sp}	Solubility product
l	Length of the conductor
λ	Wavelength
m	mole per litre of solvent
μL	Microlitre
μm	Micrometre
mM	millimole per litre of solvent
$\mu(\sigma)$	Chemical potential of solute
ν	Wavenumber in cm^{-1}
$p^x(\sigma)$	Probability of finding σ on a typical contact segment of the solute molecule
R_e	Electrolyte resistance
ρ	Resistivity
R_i	Hydrodynamic radius of a polysulfide species i
$\boldsymbol{\sigma}$	Conductivity
σ	Screening charge density
σ_n	Standard deviation indicating the width of the n-th component
T	Temperature
v	Velocity
x	Solubility of lithium polysulfide
x_i	Molar concentration
Z	Viscosity
$\mathbf{Z}$	Complex number

Table of Contents

I Background **9**

1 Introduction **10**
1.1 Rechargeable batteries for electric vehicles: an emerging need 10
1.2 Lithium-sulfur (Li-S) battery as a next-generation battery 11
1.2.1 Cell components 12
1.2.2 Working mechanism 15
1.2.3 Challenges and alternative strategies 16
1.3 Highly concentrated electrolytes (HCEs) 17
1.3.1 HCEs for Li-S batteries 18
1.3.2 Local structure of HCEs 19
1.3.3 Ion transport in HCEs 20
1.4 Scope of the thesis 20

II Experimental and computational techniques **23**

2 Experimental and computational methods **24**
2.1 Electrolyte and cathode preparation 24
2.2 Physicochemical characterisation 25
2.2.1 Densitometry and viscometry 25
2.2.2 High-performance liquid chromatography 26
2.3 Local structure assessment 28
2.3.1 Fourier transform infrared spectroscopy 28
2.3.2 Raman spectroscopy 29
2.4 *Operando* confocal Raman spectroscopy 31
2.5 Electrochemical characterisation 32
2.5.1 Coin cell assembly 32
2.5.2 Galvanostatic charge-discharge cycling 32
2.5.3 Electrochemical impedance spectroscopy 33
2.6 Computational techniques 34
2.6.1 Conductor-like screening model for real solvents 35

III Current work **37**

3 The role of anions in concentrated electrolytes for Li-S batteries **38**
3.1 Background 38
3.2 Results and discussion 39

3.2.1 Local structure and speciation . . . 40
3.2.2 Ion transport . . . 41
3.2.3 Electrochemical performance . . . 43
3.2.4 Elemental S_8 and PS solubility . . . 45
3.3 Concluding remarks . . . 46

4 Hückel anion based concentrated electrolytes for Li-S batteries 47
4.1 Background . . . 47
4.2 Results and discussion . . . 47
4.2.1 Local structure and speciation . . . 48
4.2.2 Ion transport . . . 50
4.2.3 Electrochemical performance . . . 50
4.2.4 Polysulfide solubility and modelling . . . 52
4.3 Conclusions and outlook . . . 53

5 Machine learning approaches for PS solubility prediction 54
5.1 Background . . . 54
5.2 Results and discussion . . . 54
5.2.1 Chemical potential as a molecular descriptor . . . 55
5.2.2 Data collection . . . 55
5.2.3 Regression model development and validation . . . 56
5.2.4 Multiple linear regression model building . . . 57
5.3 Conclusions . . . 58

6 Insights to PS dissolution and diffusion by *operando* Raman spectroscopy 59
6.1 Background . . . 59
6.2 Results and discussion . . . 59
6.2.1 Raman spectra at open circuit voltage . . . 60
6.2.2 Raman spectra during galvanostatic cycling . . . 60
6.2.3 Concentration-dependent PS solubility and diffusion . . . 61
6.3 Conclusions and outlook . . . 62

7 Summary and outlook 64

Appendices 66

A 67
A.1 *Operando* Raman spectra during first charge-discharge . . . 67
A.2 Deconvolution results and electrolyte properties . . . 70

B 73
B.1 Relation between solubility and chemical potential . . . 73

Bibliography 77

Part I

Background

Chapter 1

Introduction

Rechargeable batteries play a pivotal role in resolving problems of energy consumption and global warming. They can power a wide range of devices, from small smartphones and computers to large cars and trucks, thus they enable renewable energy sources to replace fossil fuels for driving us towards a cleaner and more sustainable future. Lithium-ion batteries (LIBs) – possessing high energy density and efficiency – currently dominate on the market of rechargeable batteries for powering household electronic devices and electric vehicles. However, LIBs face serious limitations including raw material shortages, safety concerns, and limited lifespan.[1] An emerging alternative is the lithium-sulfur (Li-S) battery, which promises higher energy density and lower costs, *e.g.,* on the active material – sulfur.[2] Yet, it has not been commercialized due to the challenges of lithium polysulfides (LiPSs) dissolution in the electrolyte that lead to rapid capacity fading and short lifespan.[3] This thesis thus focuses on using highly concentrated electrolytes (HCEs) to mitigate these issues, aiming to stabilize Li-S batteries and enhance their commercial viability.

1.1 Rechargeable batteries for electric vehicles: an emerging need

The world is transitioning to electric energy.[4] The relevance of electric vehicles (EVs) is twofold:[5] EVs help ease the demand for fossil fuels, such as crude oil, natural gas, and coal, which are major energy sources globally. With high fossil fuel consumption rates, oil reserves are predicted to last only 45-100 years. EVs significantly reduce greenhouse gas emissions. Internal Combustion Engine-based vehicles contribute heavily to carbon dioxide emissions, but widespread adoption of EVs can considerably lower these emissions. The demand for EVs and HEVs with lower carbon dioxide emissions is increasing due to the rise in pollutant levels and declining petroleum reserves. The production of EVs is estimated to exceed 55 million by 2037, more than doubling current production levels.[5,6]

As per the 'Global EV Outlook' report, in 2023, nearly one in five cars sold globally was electric, bringing the total number of electric cars on the roads to 40 million.[7] The transition to electromobility is accelerating in many countries world-

wide. The rapid uptake of EVs, including two-wheelers, cars, vans, trucks, and buses, continues to drive this growth.

At the heart of the current EV lies the LIBs and they dominate the EV market over other types (lead-acid, Li-S or nickel Metal Hydride).[8] As the energy density of current LIBs is approaching its limit, developing new battery technologies beyond lithium-ion chemistry and looking for novel electrode materials is of utmost importance. A battery with a high energy density is required to attain longer driving mileage.[1,9] Moreover, a higher gravimetric energy density is vital for many applications, such as aerospace, and a high volumetric energy density is more crucial for electronic devices and electric vehicle applications. Therefore, high volumetric and gravimetric energy densities will drive the development of next-generation rechargeable batteries. Li-S technology appear to be a promising energy storage system to take over from the conventional LIBs for next-generation energy storage owing to their overwhelming energy density compared to the existing LIB today.[1] Another major reason is the lower environmental profile compared to the heavy metals used in LIBs.[6]

1.2 Lithium-sulfur (Li-S) battery as a next-generation battery

A brief history of battery

The 18th century marks the first invention in electrochemistry by scientists such as Benjamin Franklin, Galvani and Alessandro Volta.[10] In 1749, Benjamin Franklin pioneered the term "battery" while experimenting with electricity, utilising interconnected glass plates. Following this, in 1798, Luigi Galvani made notable observations on the effects of electric sparks on the muscular legs of frogs, revealing the astonishing impacts of static electricity, even post-dissection. The true evolution of batteries began in 1799 when Alessandro Volta developed the first functional battery.[10]

Lithium-sulfur batteries

The first Li–S battery dates back to 1962 when Herbert and Ulam introduced the sulfur cathode concept[1,11]. Research into Li–S batteries paused after Sony commercialised LIBs in the 1990s, which offered more stable cycling performance and better safety. However, the early 2000s saw a resurgence in Li–S battery research driven by the demands of emerging applications like electric vehicles and grid energy storage as traditional LIBs approached their energy density limits.[1]

A significant breakthrough occurred in 2009 when Nazar and group used CMK-3, a type of mesoporous carbon, to create nanoscale channels for sulfur, achieving high discharge capacity and stable cycling over 20 cycles. This development sparked a renewed interest in Li–S batteries[12]. Since then, research into Li–S batteries has surged, leading to substantial progress in specific capacity and cycling performance. Figure 1.1 shows a dramatic increase in Li–S battery research from 2008 onwards, following the pioneering use of CMK-3. Between 2010 and 2024, over 10,000 publications on Li–S batteries were added, comprising about 96% of the total literature on the topic, according to the Web of Science database.

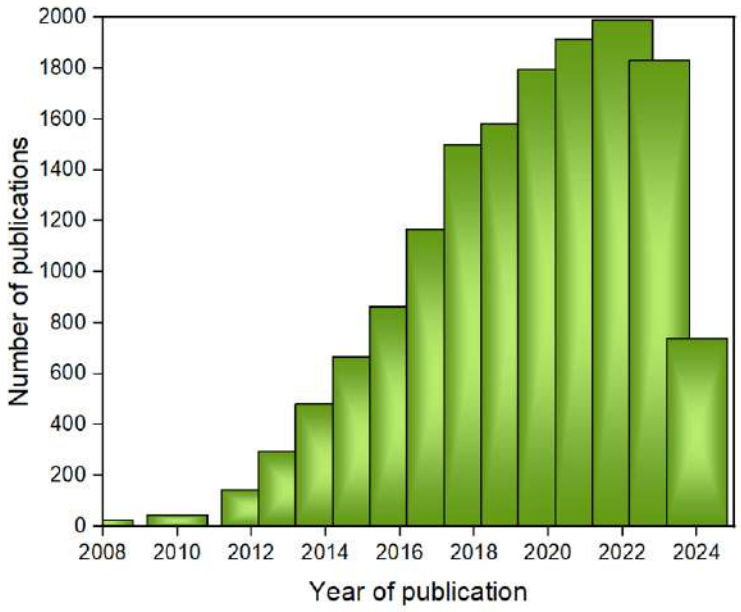

Figure 1.1: Statistics on Li–S battery publications from 2008 to 2024, obtained by searching for the term “lithium sulfur batteries” in the "topic" field on the Web of Science website. This search was conducted on 28 May 2024, accessed through: `https://webofknowledge.com/`.

Over the past years, various research projects have been developed, such as EUROLIS[13] “Advance European Lithium Sulfur cells for automotive applications” and ECLIPSE “European Consortium for Lithium-Sulfur Power for Space Environments” for manufacturing Li-S batteries.[14] Recently the creation of another European platform called homologous European project (HELIS) managed to manufacture a prototype Li-S battery capable of reaching 500 Wh/kg of energy capacity, 1000 Wh/kg of power capacity, and a life longer than 1000 cycles.[6]
Li-S Energy (ASX), an innovative Australian company, is advancing toward commercialising a decade of research on Li-S batteries.[15] Based in Brisbane and working with top researchers at Deakin University, the company has demonstrated that incorporating Boron Nitride Nanotubes[16] and its patented nanocomposite Li-nanomesh into Li-S batteries can nearly double the energy density while maintaining a similar cycle life to consumer-grade LIBs. Li-S Energy’s exceptional lab results have been validated, enabling the company to access industrial and research opportunities at the Fraunhofer Institute in Germany, Europe’s largest application-oriented research organisation.[15] In the following sections, we will explore the components, working mechanism, challenges, and our strategies for addressing the issues in Li-S batteries.

1.2.1 Cell components

A freshly assembled Li-S cell mainly comprises Li metal as an anode, elemental sulfur dispersed in a carbon source as a cathode, and an electrolyte. Other components include a current collector, binder, and separator. For any battery, the anode and cathode are supported by a current collector, which is a good conductor of elec-

tricity or collects electrons through an external circuit. For the Li metal anode, stainless steel is a current collector and provides mechanical support. The current collector for carbon-sulfur composite cathode is an aluminum foil on which the composite slurry is coated. Moreover, the lower cell voltage of Li-S (2.2 V) enables the use of aluminum without any corrosion.[17] Different binders are used to ensure proper mixing of sulfur with carbon conducting additives. Some common binders include polyvinylidene fluoride, polymethylmethacrylate, polytetrafluoroethylene and polyethylene oxide. A separator is an ion-permeable porous membrane made of polyethylene or polypropylene. It prevents direct contact between electrodes and controls damage to the cell. A separator should be thermally stable, have good wettability and have a high dielectric strength. Typical choices of separators include Celgard 2500, which is based on polypropylene-based material. Another example is the Whatman glass fibre separator.

Lithium metal anode
Lithium is the most electronegative metal (-3.0 V vs SHE). This high negative potential means high cell voltage when combined with certain cathodes. Lithium is the lightest metal in the periodic table (0.534 g/cm^3), enabling a high specific capacity of 3861 m Ah/g. Though highly reactive, lithium metal is found to be stable with a number of organic solvents. The stability is attributed to the passivation layer or the solid electrolyte interphase (SEI) on the metal surface and prevents further reactions with the electrolyte which is in contact.[18]

Sulfur-carbon composite cathodes
Sulfur is the 16^{th} most abundant metal on earth's crust.[19] It is cheap and environmentally friendly. Sulfur has a high theoretical gravimetric capacity. Sulfur is annually produced as a by-product of the desulfurisation of coal or by hydrodesulfurisation of petroleum by miners. Due to the poor electrical conductivity of elemental sulfur, it is usually mixed with carbon material. Activated carbon, carbon black, microporous carbon, and mesoporous carbon are a few examples of such carbon-based materials.[20–22]

Electrolytes
The electrolyte is a crucial component in a Li-S battery, serving as the medium for lithium-ion transport between the positive and negative electrodes. Electrolytes can be mainly categorised into liquid and solid types. Although solid electrolytes, including gel polymers and glassy electrolytes, are gaining considerable attention, liquid electrolytes remain the most extensively explored for Li-S batteries. Separators soaked with liquid electrolytes effectively penetrate the porous carbon-sulfur composite cathode and wet the lithium metal anode. The primary components of liquid electrolytes include salts, solvents, and additives. The salts, solvents and additive used in this thesis are given in Figure 1.2.

Salts: Lithium salt is the main source of Li^+ ions for the electrolyte. A salt should dissociate well in a given solvent and should form a good SEI at the strongly reducing anode and resist oxidation at the cathode. The salt should have an elec-

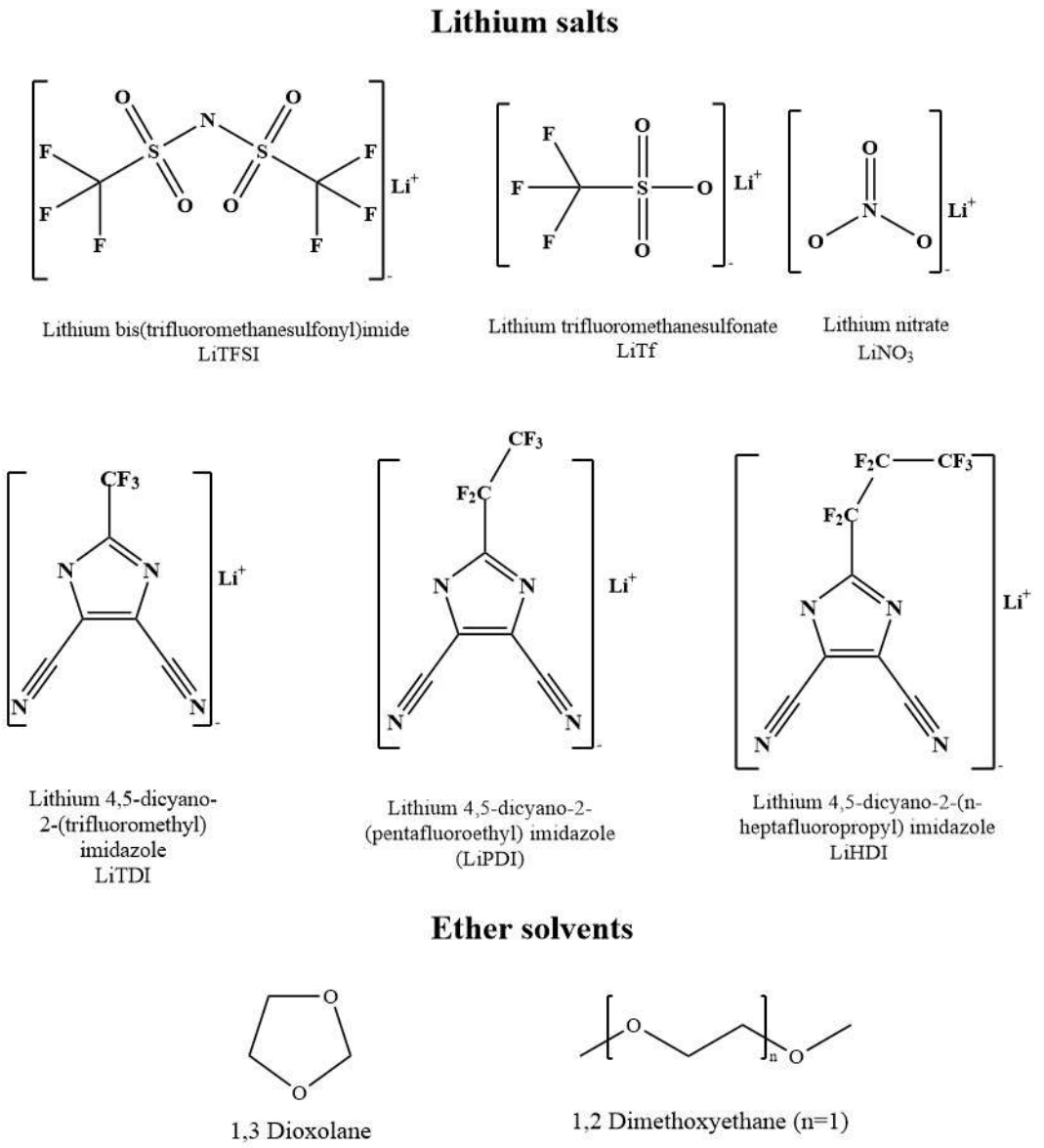

Figure 1.2: Salts and solvents used for electrolyte preparation

trochemically stable anion. The most commonly used salts in Li-S are lithium bis(trifluoromethanesulfonyl)imide ($Li[N(SO_2CF_3)_2]$, LiTFSI and lithium trifluoromethanesulfonate ($Li[SO_3CF_3]$, LiTf. They have high thermal stability and are compatible with ether solvents.[17] Recently, lithium salts based on Hückel anions are gaining attention due to their low PS solubility.[23] Hückel salts explored here are LiTDI or lithium 4,5-dicyano-2-(trifluoromethyl)imidazole ($Li[C_6F_3N_4]$, LiPDI or lithium 4,5-dicyano-2-(pentafluoroethyl) imidazole ($Li[C_7F_5N_4]$ and LiHDI, lithium 4,5-dicyano-2(heptafluoropropyl) imidazole ($Li[C_8F_7N_4]$.

Solvents: Nearly 80% of the electrolyte mass is solvent.[18,24] The solvent should have the ability to dissolve lithium salts even at high concentrations (high dielectric constant). The viscosity should be low so lithium ions can migrate easily. The solvent should remain inert or have good compatibility with all cell components

within the battery operating voltage. The solvent should be cheap and non-toxic, remain liquid for a wide range of temperatures, and have a low melting point, high boiling point, and high flash point. The solvent of choice for Li-S batteries is mainly ether based unlike the carbonate solvents used extensively for LIBs due to nucelophilic reactions with PSs.[25] Ether solvents such as dioxolane (DOL) and 1,2 dimethoxyethane (DME) are chosen because they are stable in the presence of lithium. DOL is found to be susceptible to cleavage and forms alkoxylithium fragments.[26] A binary mixture of DOL:DME was developed for its excellent rate capability at low temperature.[27] Additives: Lithium nitrate is an excellent additive to protect the lithium metal anode in Li-S batteries.[28] In the presence of nitrate, the SEI formed on the Li metal anode is less permeable to PS species due to the higher abundance of oxy-sulfur and oxy-nitrogen species.[29,30]

1.2.2 Working mechanism

A typical Li-S battery, after assembly, consists of a Li metal anode and a carbon-sulfur composite cathode separated by an electrolyte. When fully assembled, the cell has a maximum voltage known as the open circuit voltage (OCV), which is directly proportional to the difference between the electrochemical potentials of the negative and positive electrodes. During battery discharge, lithium loses electrons, or lithium ions are oxidised, and Li ions migrate in the electrolyte towards the cathode.[25]

$$\mathrm{Li} \longrightarrow \mathrm{Li^+} + \mathrm{e^-}$$

At the same time, sulfur gains electrons and undergoes reduction.

$$\mathrm{S} + 2\,\mathrm{e^-} \longrightarrow \mathrm{S^{2-}}$$

The overall reaction can be written as:

$$2\,\mathrm{Li} + \mathrm{S} \longrightarrow \mathrm{Li_2S}$$

Under normal conditions, sulfur exists as octasulfur (S_8) rings, which form a stable, orthorhombic crystal structure. Hence, the overall equation is modified to:

$$16\,\mathrm{Li} + \mathrm{S_8} \longrightarrow 8\,\mathrm{Li_2S}$$

The electrochemical reduction of sulfur mainly occurs in a three-step solid-liquid-solid conversion, as shown in Figure 1.3, and can be divided into three regions.[25]

- **Region 1 (2.4-2.1 V vs. $\mathbf{Li^+/Li^0}$):** In this region, solid elemental S_8 is transformed into higher-order lithium PSs (Li_2Sx, where $x = 8-4$), which are soluble in the electrolyte.
- **Region 2 (2.1 V vs. $\mathbf{Li^+/Li^0}$):** This region features a relatively stable voltage plateau where higher-order lithium PSs are further reduced to lower-order PSs such as Li_2S_3 or Li_2S_2.
- **Region 3 (2.0 V vs. $\mathbf{Li^+/Li^0}$):** In this final stage, the soluble Li_2Sx is converted to solid Li_2S.

At the end of discharge, reverse reactions occur, converting Li_2S back to Li and S.

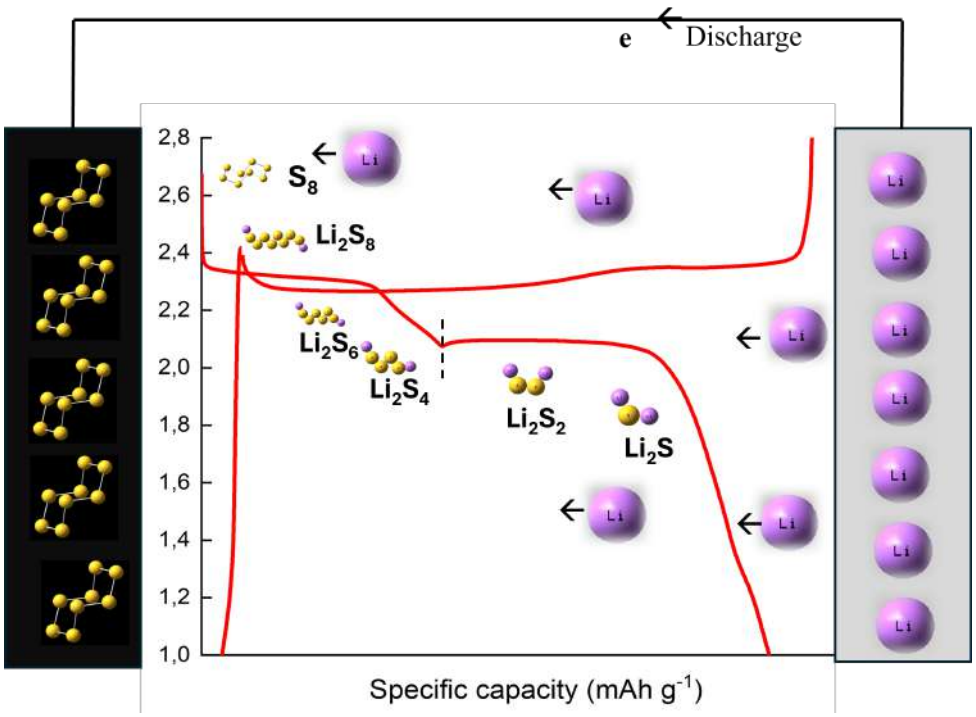

Figure 1.3: Typical Li-S battery charge-discharge curves.

1.2.3 Challenges and alternative strategies

Though Li–S batteries have the potential to deliver an energy density of 500-600 Wh/kg, several challenges exist concerning the anode, cathode and electrolyte.[31]

On the lithium metal anode side:
The highly reactive lithium metal electrodes face many challenges to the development of practical Li-S cells. During charging, dendrites grow on the anode side and can eventually result in short circuit between the two electrodes and a catastrophic thermal runaway of the cell posing safety hazards.[32] In Li-S batteries, due to the polysulfide shuttle phenomenon, soluble polysulfides can corrode the lithium electrode. Moreover, the lithium electrode may get passivated by the insoluble Li_2S_2 and/orLi_2S that are deposited on its surface. During cell operation, the passivation layer grows and results in high cell resistance and capacity fading.[33] To address these issues, protected lithium metal electrodes have been developed using additives. Lithium nitrate as an additive can prevent PS shuttling by passivating the lithium metal surface, thereby inhibiting the chemical reactions of PSs in the electrolyte with the lithium metal.[30] This is due to formation of a LixNOy film on the lithium metal surface which prevent PSs in the electrolyte from directly contacting the lithium metal.[30,34]

On the sulfur cathode side:
One of the main problems of elemental sulfur is that it exhibits very low conductivity (approximately 5×10^{-30} S/cm) at 25°C.[25] Another problem is the volume variation of the sulfur cathode during cycling. Elemental sulfur (S_8) has a density of 2.07

g/cm^3, while the final product, Li_2S, has a density of 1.66 g/cm^3, resulting in an expansion of approximately 80%.[25]

The composition and structure of the cathode plays an important role in Li-S battery performance. Carbon materials supported by binders form a conductive scaffold that allows electrochemical conversion of sulfur species through charge transfer at the conductive carbon surface.[35] Additionally, the carbon-binder scaffold provides mechanical stability in order to withstand volume changes as well as dissolution and precipitation reactions of sulfur species during charge-discharge process. Li-S battery performance can be tailored using various kind of porous and nanostructured carbons and binders as conductive cathode scaffolds.[20–22,36,37]

On the electrolyte side:
The PS dissolution and diffusion in the electrolyte influence the electrochemical utilisation of sulfur or the discharge capacity, rate capability and cycle life of Li-S battery.[33] The main challenge arises from the dissolution of high-order or long chain PSs formed in the first and second regions of discharge process (Figure 1.3). These PSs can diffuse through the separator and react with lithium metal leading to sulfur loss from the cathode side, corrosion of the lithium metal and self-discharge.[33,38] Therefore it is very important to optimise and design electrolytes to develop high performing Li-S battery.

1.3 Highly concentrated electrolytes (HCEs)

The salt concentration in commercial battery electrolytes is typically around 1 mol/L. This concentration ensures good ionic transport between the cathode and anode, as ionic conductivity increases with salt concentration up to this level. Beyond 1 mol/L, ionic conductivity decreases and viscosity increases, which are generally unfavourable for battery performance. Despite these challenges, high salt concentrations exhibit several unusual properties such as high reductive and oxidative stability, high carrier density and low PS dissolution making them a strong candidate in the battery field.[39]

Historically, the first application of HCEs was before the commercialisation of LIBs.[39] In 1985, the inhibition of solvent co-intercalation was demonstrated for a ZrS_2 electrode using a saturated $LiAsF_6$ in propylene carbonate electrolyte.[40] Later, the polymer-in-salt concept was developed using different salts ($LiClO_3$, $LiClO_4$, and $LiCF_3CO_2$) mixed with polymers such as poly(propylene oxide) and poly(ethylene oxide) to create a rubbery material with a low enough glass transition temperature to demonstrate conductivity around 10^{-4} mS/cm and an electrochemical stability window (ESW) of about 2.5 V at room temperature. Subsequently, new concepts such as water-in-salt electrolytes, solvent-in-salt electrolytes, solvate ionic liquids and localised HCEs were developed.

Classification of HCEs: Water in salt electrolytes employ very high salt concentrations, *e.g.*, >20 molal LiTFSI in water. Such high concentrations prevent the presence of “free" anions, thus overcoming the ESW limitation of water. Numerous salts have been used to create water in salt, including NaTFSI,[41] $Mg(TFSI)_2$,[42]

$Ca(NO_3)_2$,[43] and $K(C_2H_3O_2)$.[44] Non-aqueous HCEs were initially developed to replace ethylene carbonate-free electrolytes due to their poor performance in fast charging. However, EC has proven difficult to replace with organic solvents as most suffer from reductive decomposition or co-intercalation into graphite. Increasing the salt concentration enabled the use of several electrolytes, such as 2.7 M LiBETI/PC, 4.2 M LiTFSI/acetonitrile, and 4.2 M LiTFSI/dimethoxyethane with graphite electrodes. Solvate ionic liquids often involve a multidentate organic solvent, typically a glyme such as triglyme or tetraglyme, combined with an alkali salt such as LiTFSI.[45] Localised HCEs are developed by first creating a standard non-aqueous HCE and then adding a low-viscosity inactive solvent such as hydrofluoroethers. This reduces the viscosity of the HCEs by disrupting the three-dimensional network or decreasing ion-ion interactions while preserving the highly ionic solvation shell of the salt cation.[46,47]

The past decade has witnessed the application of various HCEs in batteries, including LIBs, Na-ion batteries, and Li-S batteries. The significant interest in HCEs is attributed to their unique functionalities, including their distinctive solution structure, ion transport properties, anion-derived solid-electrolyte interphase, high energy density, and high stability.[39]

1.3.1 HCEs for Li-S batteries

One promising way to address the PS dissolution problem is to increase the salt concentration in the electrolyte. Suppression of PS dissolution at high concentrations can be attributed to mainly 2 main factors:

The common ion effect: The solubility of LiPS (x) is influenced by the concentration of lithium ions present in the electrolyte due to the common ion effect. The solubility product (K_{sp}) of LiPS can be expressed as[48]:

$$Li_2S_n \rightleftharpoons 2Li^+ + S_n^{2-}$$

$$K_{sp} = [Li^+]^2[S_n^{2-}] = 4x_0^3$$

$$x_0 = \left(\frac{K_{sp}}{4}\right)^{1/3}$$

where x_0 represents the solubility of lithium PS in the absence of lithium ions in the solvent. If the concentration of lithium salt in the electrolyte (C) is significantly higher than the solubility of PS, then the solubility of PS in the concentrated electrolyte becomes:

$$\frac{x}{x_0} = \left(\frac{2x_0}{C}\right)^2$$

Thus, in the presence of a concentrated electrolyte, the solubility of lithium PS is substantially reduced.

High viscosity: The increased viscosity of HCEs hampers the diffusion of PSs, reducing their solubility. The viscosity of the electrolyte solution affects the diffusion of a bulky PS anion. The diffusion constant (D_i) of a PS ion (species i) is related to the viscosity (Z) through the Stokes-Einstein relation[48]:

$$D_i = \frac{kT}{6\pi Z R_i}$$

where R_i is the hydrodynamic radius of the PS ion, k is the Boltzmann constant, and T is the temperature. The hydrodynamic diameter is substantial for large anions, such as long-chain PS ions, resulting in slow diffusion.

In this thesis, our primary focus will be on the development of electrolytes. Specifically, we aim to increase salt concentration and explore the role of anions. Additionally, we will introduce new electrolytes aimed at reducing the dissolution of PSs in the electrolyte. The main properties explored in this thesis are described in the following sections.

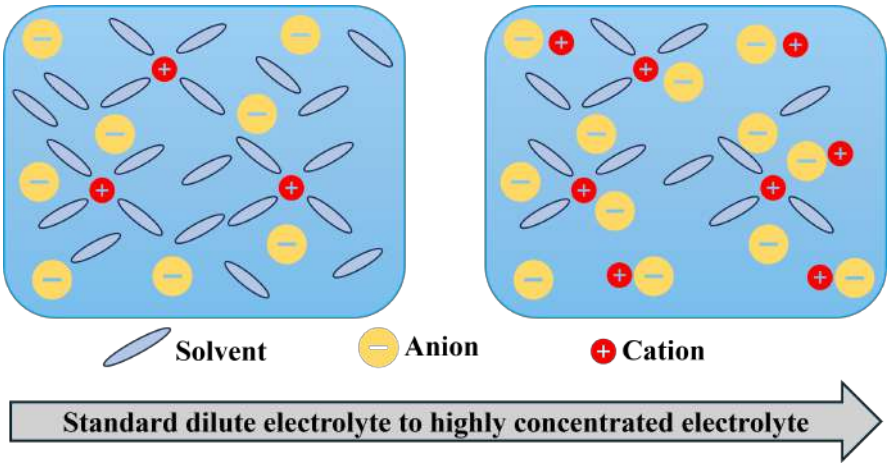

Figure 1.4: Local structure of dilute versus HCEs.

1.3.2 Local structure of HCEs

Understanding the local structure of electrolytes, from dilute solutions to HCEs is essential. As the concentration of lithium salt increases, the interactions between ions and solvent molecules change significantly. The local structure of electrolytes, ranging from dilute to highly concentrated, typically involves a lithium salt dissolved in aprotic solvents. This structure is often studied using Raman and FTIR spectroscopy (Section 2.4). These methods allow for the deconvolution of anion vibrational bands, providing insights into the various coordination modes of the anions and the relative amounts of anions with different coordinations.[49] The anion coordination modes include SSIP (solvent-separated ion pair, i.e., "free" anions), CIP (contact ion pair, i.e., an anion coordinated to a single Li^+ cation), and AGG (aggregate, i.e., an anion coordinated to two or more Li^+ cations).[49] As the concentration of lithium salt increases, the number of “free” anions, which appear at

the lowest wavenumbers, decreases, while the number of ion pairs and aggregates increases at higher wavenumbers (Figure 1.4).[50,51]

In general, the elimination of free solvent and extensive ionic association are the key factors contributing to the unusual properties of HCEs.[39]

1.3.3 Ion transport in HCEs

The main function of an electrolyte is to transport ions between the positive and negative electrodes. Generally, the salt concentration is kept at around 1 mol/L to maximise ionic conductivity, which is directly related to the local structure of the electrolyte.[39] In dilute electrolytes, there are more free anions and Li^+ cations coordinated to solvent molecules, functioning as mobile carriers. As the concentration increases, ion pairs and aggregates become predominant, leading to extensive ionic association. Though the ionic conductivity and viscosity decrease with increasing salt concentration, the choice of anion plays an important role, especially in concentrated electrolytes.

Moving from dilute electrolytes to HCEs, the ion conduction mechanism changes significantly. In dilute electrolytes, Li^+ ions conduct together with their solvation sheath $[Li(solvent)_n]^+$, following a "vehicle-type" mechanism.[52] In HCEs, due to the high number of ion pairs and aggregates, the primary ion conduction occurs via a repeated ion dissociation/association process where Li^+ dissociates from one anion and associates with another. This phenomenon is referred to as the exchange mechanism or structural diffusion[53,54], and it has been confirmed using classical molecular dynamics (MD) simulations, which highlight the importance of anion and solvent residence times in the Li^+ coordination shell.[55]

Another interesting feature at high concentrations is the high transference number reported previously[56] as HCEs enable a high Li^+ flux between the electrodes. The transference number values often seem to differ depending on the measurement method, such as the electrochemical method or pulse-field gradient spin-echo nuclear magnetic resonance and further verification is required.[39]

1.4 Scope of the thesis

The current work aims to prepare and investigate electrolytes using various salts up to their maximum solubility in the most common solvent mixture in Li-S batteries. Specifically, the study focuses on two main categories of salts: LiTFSI and LiTf based salts, and Hückel type or imidazolium salts such as LiTDI, LiPDI, and LiHDI. The literature has previously reported using LiTf and LiTDI at maximum concentrations of 3 mol/L and 1 mol/L of solvent, respectively. Our study explores five different salts, from the standard 1 mol/L to their maximum solubility in the DOL:DME mixture, to formulate various concentrated electrolytes.

The motivation for testing concentrated electrolytes in Li-S batteries stems from the remarkable results observed with 7 mol/L of LiTFSI in DOL solvent mixture, which yielded a high capacity of over 800 mAh/g and nearly 100% coulombic efficiency.[56] The unusual properties of high-concentration electrolytes (HCEs), such

as their ability to reduce PS solubility and their unique solution structure and ion-transport characteristics, played a key role in understanding the behaviour of concentrated electrolytes based on various salts.

Our study utilised common salts in Li-S batteries, including LiTFSI, LiTf, and Hückel salts synthesised at WUT (LiTDI, LiPDI, and LiHDI). Solutions with high salt solubility were prepared: 1-7 mol/L for LiTFSI, 1-5 mol/L for LiTf, and 0.3-2.0 mol/L for Hückel salts in the DOL mixture. The aim is to provide fundamental structural and mechanistic insights into the role of the lithium salt anion in different HCEs and less concentrated electrolytes. The study rationalises the physicochemical properties and electrochemical battery performance using local structure analysis and speciation, including PS solubility.

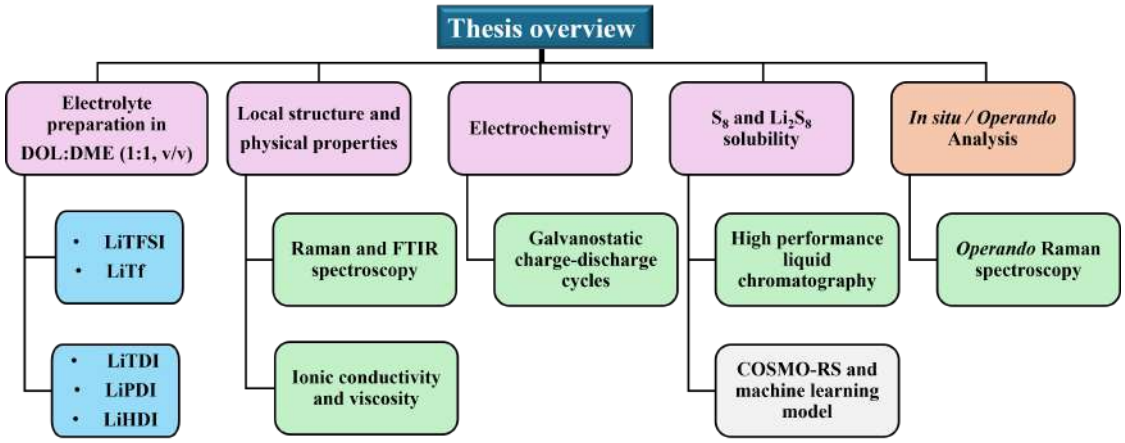

Figure 1.5: Scope of the thesis.

- Chapter 1 provides an overview of batteries, the need for rechargeable batteries, and introduces the Li-S battery as a prime candidate among next-generation batteries. It discusses the different cell components in Li-S batteries, along with the associated challenges and alternative strategies to address them. HCEs are introduced as a potential solution to the problem of PS dissolution, highlighting their unique properties.

- Chapter 2 details the experimental and computational methods used to investigate the electrolytes. It covers the preparation of electrolytes and cathodes and various physicochemical and electrochemical characterisations. To predict PS solubility, a computational tool called COSMO-RS is employed alongside a multiple linear regression model. *Operando* Raman spectroscopy is utilised to gain deeper insight into PS diffusion.

- Chapter 3 describes the current work, which uses a combination of experimental and computational approaches to investigate electrolytes based on LiTFSI, LiTDI, and LiTf dissolved in a DOL:DME mixture up to each system's maximum salt solubility. The study compares common salts with the Hückel salt LiTDI, focusing on the role of anions. Various physicochemical and

electrochemical properties are examined, including ionic conductivity, density, viscosity, speciation, and cycling tests, to gain a fundamental understanding of electrolyte.

- Chapter 4 explores the current work on the family of Hückel salts- LiPDI, LiHDI based on the best-performing system from Chapter 3, i.e., LiTDI in DOL:DME. The main aim here was to compare the various properties in electrolytes which only differ in chain length. The local structure as a function of salt concentration is elucidated using Raman and FTIR spectroscopy, correlated with ion transport properties and electrochemical performance. PS solubility predictions are made using COSMO-RS combined with a multiple linear regression model.

- Chapter 5 describes the development of supervised machine learning approaches with COSMO-RS-based descriptors to build a regression model for PS (Li_2S_8) solubility. This tool can be applied to large electrolyte systems to obtain results close to experimental values, reducing human effort and time-consuming experiments.

- Chapter 6 deeply explores electrolyte salt concentrations' impact on PS solubility and diffusion behaviour using *in situ/operando* Raman spectroscopy.

- Chapter 7 summarises the main conclusions obtained from the extensive study of various concentrated electrolytes and their ability to suppress PS solubility through experiments and calculations. It also discusses potential future research directions.

This comprehensive investigation aims to deepen the understanding of concentrated electrolytes in Li-S batteries and explore the potential of different salts to improve battery performance.

Part II

Experimental and computational techniques

Chapter 2

Experimental and computational methods

To investigate electrolytes for lithium-sulfur batteries, we began by preparing the electrolytes by adding an appropriate amount of salts to the solvent mixture, followed by cathode preparation (Section 2.1). Next, we measured the physicochemical characteristics such as density, viscosity, and elemental sulfur solubility (Section 2.2). The local structure of the electrolytes, which provided insights into the ionic association of the salts, was elucidated using Raman and FTIR spectroscopy (Section 2.3).

Additionally, *in-situ* Raman spectroscopy was conducted to thoroughly investigate the Li–S battery during cycling (Section 2.4). For electrochemical studies, we assembled a coin cell with a lithium metal anode, the prepared electrolyte, and a cathode. Battery cycling was performed using galvanostatic charge-discharge cycles, and ionic conductivity was measured using electrochemical impedance spectroscopy (Section 2.5).

For optimal electrochemical performance of Li-S batteries, the lithium PS solubility determination was necessary. To predict the Li_2S_8 solubility, we used a conductor-like screening model combined with a multiple linear regression model (Section 2.6). The following sections of this chapter detailed the theory behind each technique and the procedures for conducting each measurement.

2.1 Electrolyte and cathode preparation

LiTDI, LiPDI and LiHDI was synthesised as reported previously.[57] LiTFSI (99.9%) was purchased from Solvionic, while LiTf (99.8%), DOL (99.8%), DME (99.8%) and S_8 (99.8%) were all purchased from Sigma-Aldrich. The salts were dried at 140° C under vacuum overnight before use. All salts and solvents were handled in an argon-filled glove box at all times (< 1 ppm H_2O). The electrolytes were made by preparing a DOL:DME (1:1, v/v) solvent mixture and dissolving (using a magnetic stirrer for 24 h at room temperature) appropriate amounts of salts to get the desired concentrations, *i.e.,* 1-7 m LiTFSI, 0.3-2 m LiTDI, 0.3-2 m LiPDI, 0.3-2 m LiHDI and 1-5 m LiTf. The highest concentrations are based on the maximum salt solubilities (here, 1 m refers to 1 mole of salt per litre of solvent).

For the electrochemical cell materials and components, the anode lithium metal foil was 200 μm thick (Honjo metal), while the C/S composite cathode was composed by sulfur, 60 wt%, (Sigma-Aldrich, 99.998% trace metal basis), carbon black (Vulcan) as conductive additive, 38.5%, and sodium carboxymethyl cellulose (Na-CMC, Mw=700,000, Sigma-Aldrich) as binder, 1.5 wt%. Appropriate quantities of sulfur and carbon black were mixed in mortar to prepare the electrodes. Then the binder was added, and the solution was mixed magnetically to obtain a homogenous slurry. The electrode suspension was cast on a 20 μm aluminum foil (Hohsen) using the Doctor Blade technique, resulting in a coating with a thickness of 250 μm. After coating, the electrode was dried at 60°C under vacuum for 24 h.

2.2 Physicochemical characterisation

The physicochemical properties density, viscosity and sulfur solubility of different electrolytes were measured using densitometry, viscometry and high-performance liquid chromatography. The methods are described below.

2.2.1 Densitometry and viscometry

The densities and viscosities were recorded for 10-50° C at an interval of 10° C using an Anton Paar DMA4500M density meter equipped with a Lovis 2000M rolling ball viscometer module. The temperature accuracy was ±0.02° C and it took approximately 5 minutes to reach equilibrium. Prior to the measurements, the instrument was calibrated and verified using standards. Sample filling was performed very carefully to avoid bubbles.

Densitometry: Density measurement is important for electrolytes, especially concentrated electrolytes, to determine the weight of the electrolyte for battery applications. DMA 4500M density meter measures viscosity in the range 0-3 g/cm^3 with an accuracy of up to 5 digits. The electrolyte sample is placed in the U-shaped borosilicate glass tube, which vibrates at its characteristic frequency depending on the mass of the sample. Using this frequency and few mathematical equations, the density of the sample is measured.[58]

Viscometry: Viscosity is defined as the resistance of a liquid to flow due to internal friction. Battery electrolytes typically have a lower viscosity to ensure good ionic conductivity between electrodes. Increasing salt concentration raises the electrolyte viscosity. Viscosity measurement in our work was carried out using an Anton Paar Lovis 2000M/ME rolling ball viscometer, which operates in the range of 0.3–10,000 mPa.s.

A capillary is first filled with the electrolyte and a steel ball. The instrument operates based on the rolling ball motion in a capillary according to Hoeppler's principle[59], which states that the viscosity of a Newtonian liquid can be measured by the time required for the ball to fall under gravity through a sample-filled tube inclined at an angle. The viscosity is calculated from the time taken for the ball to roll through the electrolyte sample at an inclination angle of 15-80°. Final viscosity values were obtained by averaging the results from at least 5 back-and-forth runs of the rolling ball.

2.2.2 High-performance liquid chromatography

The solubility of sulfur in the electrolytes was determined using high-performance liquid chromatography (HPLC). In this technique, the components can be separated due to differences in the partition coefficients (distribution) of the solutes between the mobile phase (solvent or mixture of solvents under high pressure) and the stationary phase (high porosity particles in a column). HPLC is generally classified into normal-phase HPLC (where the stationary phase is polar and the solvent is non-polar) and reversed-phase HPLC (where the stationary phase is non-polar and the solvent is polar). In this thesis, we used a reverse-phase HPLC column.

The main components of HPLC include a high-pressure pump, an injection device, a column, a detector, and a recorder (Figure 2.1).[60] The liquid electrolyte containing sulfur is injected at the top of the column using a syringe. In the HPLC column, S_8 (the non-polar analyte) is distributed between the non-polar stationary phase (alkyne-C_{18} bonded with silica) and methanol (the polar mobile phase) to reach equilibrium based on the partition coefficient, thus, S_8 diffuses between the polar and non-polar phases.

The solute, along with methanol, leaves the HPLC column and enters a flow cell of a diode array detector (DAD) located perpendicular to the ultraviolet (UV) light beam. As the composition of the solution in the cell changes due to S_8 reaching it, the absorbance also changes. This enables the spectrophotometric detection of S_8, which results in a peak in the chromatogram at around 8 minutes. The retention time of the solute is the basis for its identification. The initial peak, appearing at 2 minutes (a column void time), corresponds to the elution of cations/anions.

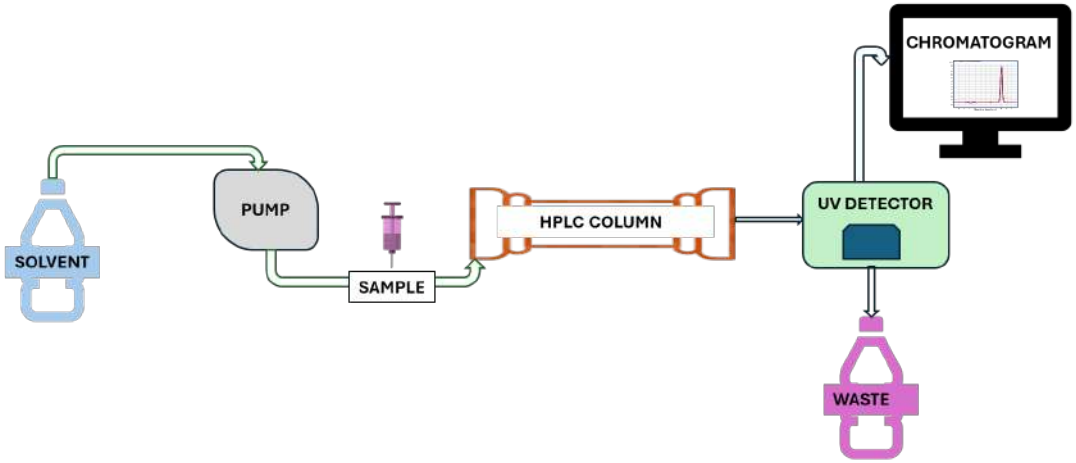

Figure 2.1: Instrumentation of HPLC

Sample preparation: The method/protocol for the high-performance liquid chromatography with spectrophotometric detection (HPLC-DAD) experiments was based on the literature.[61] A 5.46 mM S_8 stock solution was prepared by dissolving 0.0070 g S_8 in 5.0 mL DME. The stock solution was then diluted to provide the standard solutions of 2.184 mM, 0.4368 mM, 0.0873 mM and 0.0174 mM (Figure 2.2). The S_8 saturated solutions were made by dissolving 0.1 g of elemental S_8 into a sample vial with 2.5 mL of target electrolyte or suitable solvent. After being sealed and shaken

for 96 hours, the solution was allowed to rest for 72 hours. The clear solution at the top was filtered through a PTFE syringe filter (pore size 0.2 μm) and the filtrate after dilution was used for the analysis.

Instruments: An Agilent 1100 quaternary pump (Agilent Technologies) was used to deliver 100% methanol of LC-MS grade (POCH, Gliwice, Poland) through an HPLC column Zorbax SB-C_{18} (Agilent Technologies, 4.6×150 mm, 3.5 μm) with an analogous precolumn at a flow rate of 0.5 mL min^{-1} using an isocratic elution. A 7725i Rheodyne manual injector was used to inject 20 μL of each sample, and a 1100 diode array detector (DAD) from Hewlett-Packard was operated at 219 and 264 nm. The total HPLC running time was 12 minutes. UV spectra were collected in the 200-300 nm range.

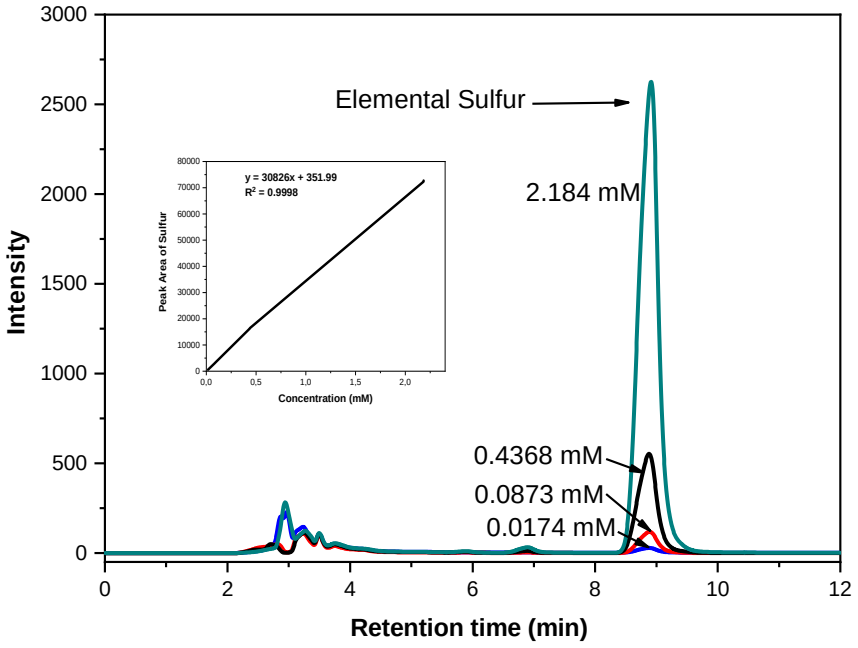

Figure 2.2: The calibration curve and chromatograms of different elemental sulfur standards at 219 nm

Analysis of standards: For quantification of sulfur in the electrolytes, a calibration curve is required (Figure 2.2). The calibration curve was obtained for standard solutions with different concentrations of elemental sulfur S_8 in the range from 0.0174 mM and 2.184 mM by plotting the area of chromatographic peaks corresponding to sulfur versus its concentration.[61] As the concentration of sulfur increases, the area under the peak increases. The determined calibration curve equation was used to determine the sulfur concentration in the electrolyte solutions.

2.3 Local structure assessment

Raman and infrared (IR) spectroscopy are both essential for fully measuring the vibrational modes of a molecule. Molecular vibrations that change bond length are known as stretching vibrations, which can be further divided into symmetric stretching (in-phase) and asymmetric stretching (out-of-phase). Other vibrations cause changes in bond angles, known as bending vibrations, which arise from deformation, rocking, wagging, or twisting of the bonds.[62]

Some molecular vibrations can be active in either Raman or IR spectroscopy. Generally, Raman spectroscopy yields the best results for symmetric vibrations of non-polar groups, while IR spectroscopy is more effective for detecting asymmetric vibrations of polar groups[63]. Both techniques are invaluable for capturing changes in coordination structure with variations in salt concentration in electrolytes. The molecular vibrations of the electrolytes discussed in this thesis are listed in Table 2.1.

Table 2.1: Major vibration assignments and corresponding frequencies discussed in this thesis.

Assignments	**Frequencies (cm^{-1})**	**ref**
S−N−S bending vibration	741-747	[49]
SO_3 symmetrical stretching vibration	1130-1142	[64]
CF_3 symmetric deformation	750-771	[64]
C−N stretching vibration	2228-2240	[65]
C−N-Im ring stretching vibration	1310-1320	[65]
N−C−N bending vibration	979-990	[65]

2.3.1 Fourier transform infrared spectroscopy

Fourier transform infrared (FTIR) spectroscopy measures transitions between molecular vibrations induced by the absorption of IR radiation. The absorption of monochromatic radiation by a sample follows Beer-Lambert's law, where the absorbance of a solution is directly proportional to the concentration of the absorbing material and the path length. FTIR spectra are obtained using an interferometer.[66] The IR radiation emitted from the source passes through a beam splitter and multiple mirrors, creating an interference pattern of all wavelengths before interacting with the sample. As the sample interacts with all wavelengths simultaneously, the interference pattern changes over time. Fourier transformation converts this time-domain interference pattern into the frequency domain, allowing the recording of absorbance as a function of wavelength.[66]

One condition for molecules to be IR-active is that they must undergo a change in dipole moment during vibration. Examples of IR-active molecules include HCl, NO, and CO.[63]

The unit for IR spectroscopy is the wavenumber (ν) in cm^{-1}, defined as the number of waves in a length of 1 cm, given by:

$$\nu = \frac{1}{\lambda} = \frac{v}{c} \tag{2.1}$$

where v is the velocity, λ is the wavelength, and c is the speed of light.

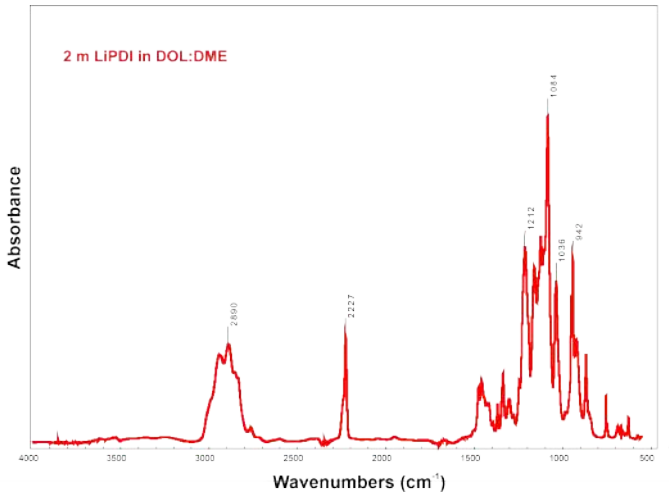

Figure 2.3: FTIR spectrum of 2 m LiPDI in a solvent mixture of DOL:DME (1:1, v/v)

FTIR spectrum of 2 m LiPDI in DOL:DME is shown in Figure 2.3.

FTIR spectra in this thesis were obtained using a Nicolet Avatar 370 spectrometer at a resolution of 1 cm^{-1}. The samples were in the form of thin films placed between two NaCl plates. The absorbance is plotted against the wavenumber to obtain the infrared spectrum shown in Figure 2.3.

2.3.2 Raman spectroscopy

Raman spectroscopy serves as a valuable tool to elucidate the cation-anion coordination structure in electrolytes with increasing salt concentrations. At higher concentrations, Li^+ and anions form ion-pairs and aggregates, while in dilute electrolytes, cation-anion interactions are negligible due to Li^+ being fully solvated with organic solvent molecules and the presence of "free" delocalised anions.[67] The fundamental principle of Raman spectroscopy lies in the interaction of incident light of a specific wavelength with a sample or molecule. When a sample is irradiated with monochromatic light in the visible region, the light can be reflected, absorbed, transmitted, or scattered.

Light scattering occurs in two forms: elastic and inelastic scattering (Figure 2.4).[63]

- **Elastic scattering**, also known as Rayleigh scattering, happens when the incident and scattered light have the same frequency. During this process, an electron at a specific vibrational or rotational level absorbs energy, transitioning to a virtual energy state with energy E_1 given by $E_1 = h\nu_1$. Subsequently, the electron relaxes and returns to its original energy level, emitting another photon with energy $E_2 = h\nu_2$ if it returns to the same vibrational level.

- **Inelastic scattering**, commonly referred to as Raman scattering, occurs when a small fraction of scattering happens inelastically. This occurs when an electron, after being excited, returns to a different vibrational level, emitting a

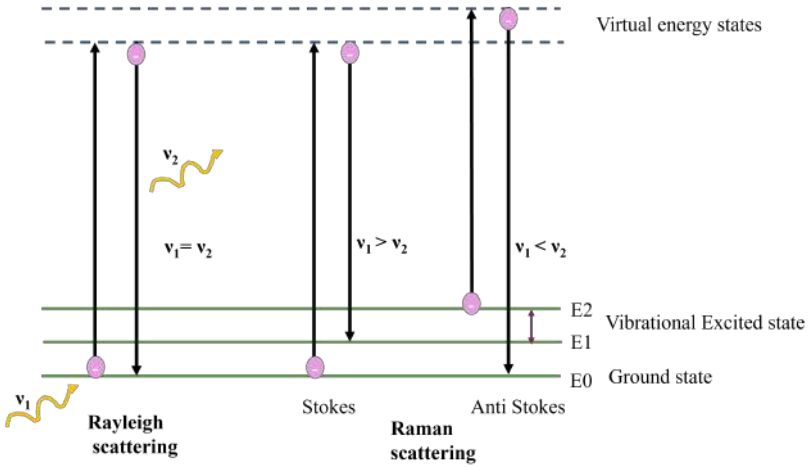

Figure 2.4: Energy level diagram for elastic and inelastic scattering.

photon with a different frequency. Raman scattering includes Stokes scattering ($\nu_1 > \nu_2$) and anti-Stokes scattering ($\nu_1 < \nu_2$).[63]

In general, Raman scattering predominantly refers to Stokes scattering at room temperature, as anti-Stokes scattering is less likely to occur.

For our Raman spectroscopy measurements, electrolyte samples (0.5-1 cm^3) were sealed in 4 cm^3 glass vials. Spectra were collected using a Nicolet Almega Raman dispersive spectrometer with a diode laser excitation wavelength of 532 nm and a spectral resolution of 2 cm^{-1}.

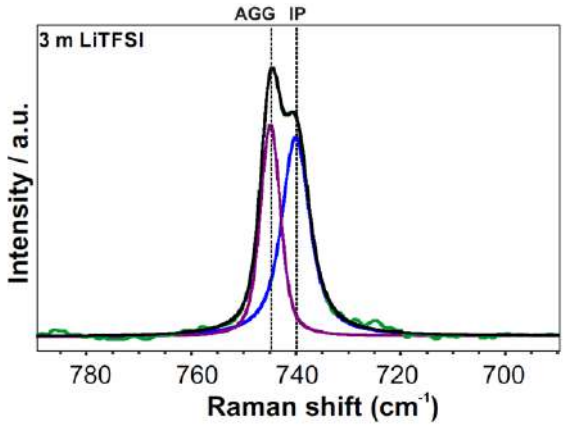

Figure 2.5: An example (3 m LiTFSI) of spectra fitting and deconvolution using Voigt functions.

Data analysis: Spectral deconvolution was performed using OMNIC software (OMNIC, Thermo Scientific) with Voigt functions. An illustrative example of deconvolution for a 3 m LiTFSI in the DOL:DME system is presented in Figure 2.5. Species were centered at 739 cm^{-1} for "free" anions, 741 cm^{-1} for ion-pairs (IP), and 747 cm^{-1} for aggregates (AGG).

2.4 *Operando* confocal Raman spectroscopy

During Li-S battery charge-discharge cycles, the lithium PSs produced dissolve in the electrolyte, leading to poor cycling stability, energy loss, and capacity decay.[68] It is very crucial to identify the type and concentration of Li_2Sx formed in different electrolytes during the cell cycling. To investigate the reaction mechanisms inside a Li-S cell, *operando* confocal Raman spectroscopy is a valuable tool since elemental sulfur and PSs are strongly Raman active.[69] The primary reason for using *operando* Raman in our studies is to compare and evaluate the LiPS evolution in Hückel salts and conventional LiTFSI in ether solvents. Our *operando* Raman measurements were performed using a confocal experimental configuration with a commercially available EL-cell. The scattered photons from the incident laser are collected from the focal plane, allowing the probing of the electrolyte or the electrode surface.[70]

Li-S *operando* cell setup

The Li-S battery was assembled in an electrochemical cell ECC-Opto-Std (EL-cell® GmbH) in a sandwich configuration similar to coin cell assembly (Figure. 2.6). The cell included a 10 mm C/S composite electrode containing approximately 1 mg of sulfur, one layer of glass fibre separator (Whatman™ 1821 GF/B, 675 μm) containing 60 μL of electrolyte, and a 15 mm counter and reference electrode of lithium metal with a 2 mm hole at the center. The cell used a borosilicate glass window for observing Raman spectra. The assembly was performed in an Ar-filled glove box with O_2 and H_2O levels controlled below 1 ppm. Galvanostatic measurements were performed at a C/10 rate (1 C = 1672 mA h/g) on a GAMRY Series G 300 at room temperature, cycling between 1 and 3 V versus $Li^+/Li°$.

Figure 2.6: Schematic view of an *operando* Raman setup.

***Operando* confocal Raman cell**

All Raman spectra were collected on a LabRam HR Evolution (Horiba GmbH) in confocal mode using a 633 nm He-Ne laser operated at a power of approximately 10 mW, a 300 grooves/mm grating, a 10X objective, a 200 μm confocal hole, and a Syncerity OE detector operated at room temperature. The laser beam was focused on the separator surface very close to the edge of the hole in the Li anode, and a neutral density (ND) filter was used to reduce the emitted laser intensity on the sample surface to 25%. Each spectrum was obtained by co-adding 30 accumulations of 20 s exposure, collected over a total period of 610 s. Baseline correction

was applied using a polynomial function to remove photoluminescence background. All calculations for analyzing the Raman spectra were performed with MATLAB (version R2023b, The MathWorks, Inc.).

Spectral analysis: The PS regions (400-600 cm^{-1}) were analysed by fitting a linear combination of Gaussian functions:

$$A(v) = \sum_{n=1}^{N} A_{n,\max} e^{-\frac{(v-v_n)^2}{2\sigma_n^2}} \quad (1)$$

Here, $A(v)$ represents the absorbance at a specific wavenumber v, $A_{n,\max}$ denotes the peak absorbance of the n-th Gaussian component centered at wavenumber v_n, and σ_n is the standard deviation, indicating the width of the n-th component. Spectral deconvolution on a series of time-resolved spectra began with the initial adjustment of absorbances at 450 cm^{-1} to zero. The absorbance values were then normalised to the C–O bond absorbance of DOL at 910 cm^{-1} before baseline correction was applied using a simple linear function. The optimisations of Gaussian parameters were calculated using non-linear least square methods in MATLAB (version R2023b, The Mathworks, Inc.).

2.5 Electrochemical characterisation

To perform the Li-S battery cycling, a coincell was assembled followed by a galvanostatic (constant current) charge-discharge cycling. For measuring the ionic conductivity of different electrolytes we performed a potentiostatic electrochemical impedance spectroscopy which are explained in sections below.

2.5.1 Coin cell assembly

For the battery tests, coin cells were assembled in the order as shown in Figure. 2.7. The coin cells (CR2032) mainly comprises a C/S composite cathode (13 mm), a lithium metal foil anode (14 mm), and a Whatman glass fibre filter (16 mm) separator filled with 80 μl of electrolyte (or 25 μl /mgS). The Whatman glass fibre filter (675 μm) prevent any electrical contact between cathode and anode while their porous structure is filled with electrolyte to allow fast ionic conduction. The cell contains two caps of stainless steel (A and H) that serve both as a sealed container and as current collectors and the spring is used to maintain a balanced pressure in the cell. The cell assembly is carried out using coin-cell crimper (Hohsen) and was assembled inside the argon-filled glovebox. The coin cell is relatively easy to build, and the effective sealing allows for reduced evaporation of the solvents

2.5.2 Galvanostatic charge-discharge cycling

The amount of charge stored in a battery or the capacity is determined using galvanostatic charge-discharge mode i.e., the current is kept constant for the charge and discharge regimes between two voltages.[71] The charge and discharge current of a battery is normally expressed as C rate. C rate is the rate at which a battery

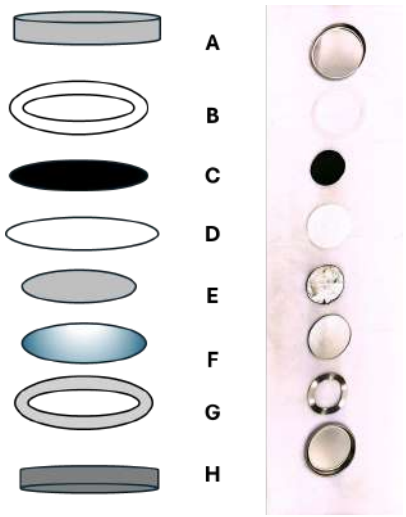

Figure 2.7: schematic view of a CR2320 coin cell: A, stainless steel can; B, polypropylene gasket; C, carbon-sulfur composite (+) cathode; D, Whatman glass filter wetted with the electrolyte; E, lithium foil anode; F,stainless steel spacer disk; G, stainless steel wave spring; H, stainless steel cap; the picture on the right is the top view from glovebox.

charge or discharge. A C rate of 1 C implies a charge and discharge of battery occurs in 1 hour, C/10 or 0.1 C equals to 10 hours and C/30 or 0.033 C rate is equal to 30 hours. For the Li-S battery tests, the initial C rate was set at C/30, and thereafter, the cycling was conducted at C/10 (1 C = 1672 mAh/gS). At higher C rate some energy can be lost into heat which lowers the capacity.

For the battery tests, the voltage limit was set between 1 and 3 V $Li^+/Li°$. The Li-S galvanostatic charge-discharge cycles were tested with a battery analyzer - Scribner Associates Incorporated 580 Battery Test System. An example of a discharge-charge cycle using C/30 C rate is shown in the introduction chapter Figure. 1.3 .

2.5.3 Electrochemical impedance spectroscopy

Electrochemical impedance spectroscopy (EIS) is a powerful tool to study ionic conductvity of the electrolytes. In EIS, a small alternating voltage (5 mV) is applied to an electrochemical cell over a wide range of frequency typically from milli Hertz to mega Hertz.[72] The applied voltage should be small so that the current and voltage are linear to each other. The sinusoidal response of the system (current) towards the applied perturbation can be expressed as a complex number Z which is given by[73]:

$$Z = a + ib$$

where a is the real part on the x axis and b is the imaginary part on the y axis and i is the imaginary unit, i^2=1. A nyquist plot graphically represent the imaginary part of impedance against the real part and a Randles circuit model fits to various parameters such as double layer capacitance (Cdl), electrolyte resistance (Re), charge transfer resistance (Rct)and a warburg element (W) given in Figure. 2.8. The

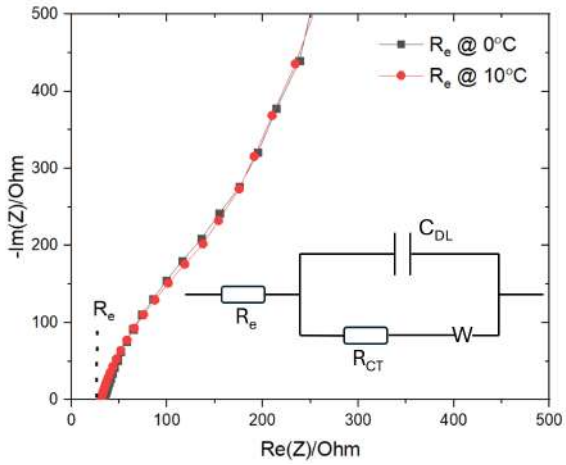

Figure 2.8: Schematic representation of an electrochemical system's response to a low-amplitude (5 mV) sinusoidal signal for the 1 m LiHDI in DOL:DME electrolyte at 0 and 10° C.

electrolyte resistance (Re) is shown in the figure for the 1 m LiHDI in DOL:DME at 0 and 10 ° C. Re depends on several factors such as salt concentration, type of ions and geometry of area in which current is carried.

The resistance Re of a conductor with resistivity ρ is given by

$$Re = \frac{\rho l}{A}$$

where ρ is the resistivity, l is the length of the conductor, and A is the cross-sectional area.

When replacing resistivity ρ with conductivity σ and cell constant

$$C = \frac{l}{A}$$

the equation becomes

$$\sigma = \frac{C}{Re}$$

where σ is the conductivity of the material. Conductivity has SI units of siemens per metre (S/m).

Inorder to measure the ionic conductvity, the electrolytes were first placed into micro conductivity cells with cell constants values = 0.3-0.7 cm^{-1}, which were then put into a cryostat-thermostat system (Haake K75 with the DC50 temperature controller). A cryostat is essential to measure the ionic conductivities for a temperature range of 0-50° C at an interval of 10° C, with a thermal equilibration of at least 30 min. The cryostat is connected to the VMP3 potentiostat from biologic and an A.C. signal of 5 mV in 500 kHz to 10 Hz range with 10 points per decade was applied.

2.6 Computational techniques

Modelling has become very popular in all fields of research including batteries. Machine learning (ML) approaches are widely applied to LIBs[74], and these are different

ongoing projects such as BIG-MAP[75], Faraday institution[76] and Battery 2030+[77] aimed to solve many practical challenges and to optimise the battery production. Computational approaches can be effectively applied to optimise various electrolyte designs. In this work, we use molecular / computational modelling to predict the Li_2S_8 solubility in the electrolytes.

For the solubility prediction, we apply a multiple linear regression (MLR) model to develop a quantitative structure activity relationship (QSAR) model correlating molecular descriptor $\mu(\sigma)$ computed from a conductor-like screening model with the experimental Li_2S_8 solubility. A detailed explanation of the MLR model and the solubility prediction is provided in Chapter 6. The next section explains the COSMO-RS model used in the current work.

2.6.1 Conductor-like screening model for real solvents

The conductor-like screening model for real solvents (COSMO-RS)[78,79] is an efficient method for predicting the thermodynamic properties of compounds in the condensed phase.

Molecular interactions in condensed phase: The condensed phase is characterised by strong interactions between closely held molecules. The main interactions in the condensed phase are van der Waals interactions, Coulombic or electrostatic interactions, and hydrogen bonding. Molecular interactions described using dielectric continuum models do not efficiently account for the intense electric fields or polarisation of solvents on the molecular surfaces of solutes. On the other hand, COSMO-RS starts with the assumption that a solute X can be screened by a solvent molecule with the same energy as it would be screened by a conductor. This screening is termed "conductor-like" because the solvent can offer the opposite ideal surface charges for all faces of the solute molecule as effectively as a conductor. Deviations from ideal screening are captured as pairwise interactions of misfit charges on the contact areas between molecules.[80]
Analysis of the screening charge densities: In COSMO-RS, molecules are considered as typical contact segments. By analyzing the surface charge densities over these contact segments, the effective probability $p^x(\sigma)$ of finding a screening charge density σ on a typical contact segment of the solute molecule can be obtained. This probability function is known as the σ profile and it is characteristic not only of a single molecule but also of an ensemble of solvent molecules. For solvents with different constituents at different molar concentrations. The σ profile is given by the weighted sum of the σ profiles of the components. COSMO-RS can also be used to calculate the chemical potential $\mu(\sigma)$ of solutes in various solvents, essential for understanding solubility and reactivity.[81]
Steps for a COSMO-RS calculation: There are two main steps for a COSMO-RS calculation (Figure 2.9)[82]. In the first step, we perform geometry optimisation of different molecules and use COSMO for quantum chemical calculation to obtain the screening charge density (σ) on the molecular surface. In the second step, the quantum chemical output is used to obtain thermodynamic properties such as vapor

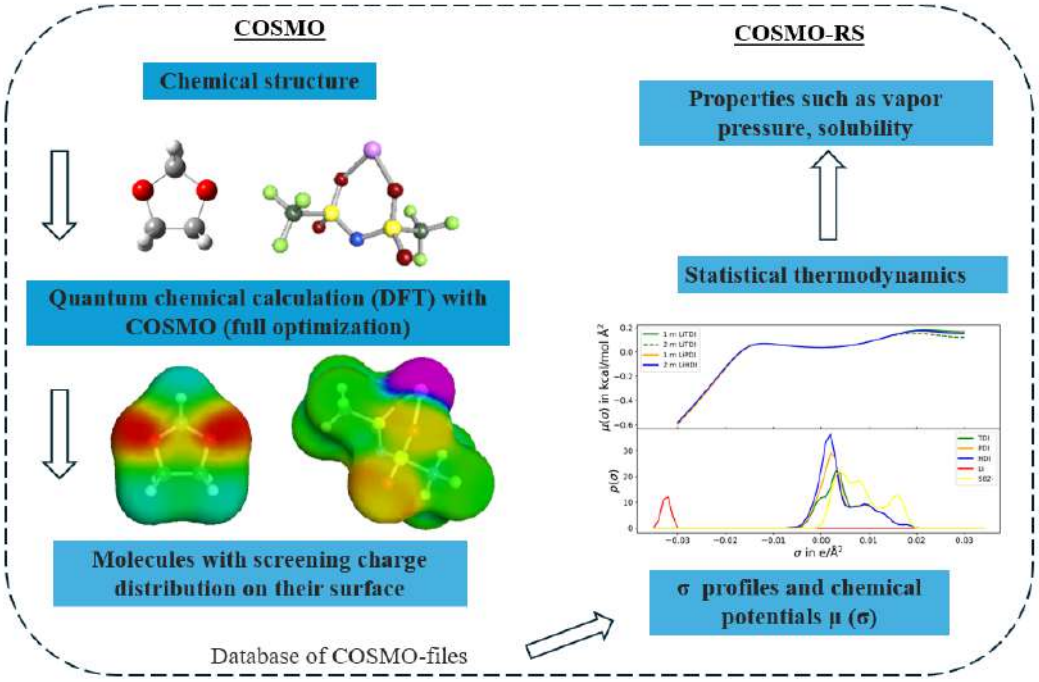

Figure 2.9: Workflow of COSMOtherm calculation. Inspired from reference[82].

pressure, solubility, phase equilibrium, and activity coefficient. The detailed treatment of electrostatic interactions and the efficient handling of dielectric boundary conditions make COSMO-RS a powerful modeling tool for understanding solution chemistry in complex systems.

In this thesis, we use COSMO-RS model[78,79] to predict the solubility of Li_2S_8 in the electrolytes. The COSMO-RS calculations[78,79] were conducted using the COSMOthermX program and the BP-TZVPD-C30-1701 parameterisation at 293.15 K temperature.[83]

The TURBOMOLE V7.1 software package[84] was used for initial geometry optimisation of the molecules using density functional theory (DFT)[85,86] This was done using the BP86 functional and the TZVP basis set in both the gas phase and assuming a perfect conductor ($\epsilon = \infty$). Additionally, single-point calculations were performed using BP86/TZVPD to generate a fine grid cavity. The molecular structures and cosmo-files for cycloS_8, TFSI, Tf, TDI, PDI, HDI, DOL and DME were obtained using the TmoleX 4.6.0 graphical user interface and were added to the COSMOthermX database. All COSMO-RS computations were performed for all concentrations of the electrolytes made with LiTFSI, LiTf and LiTDI in DOL:DME (1:1, v/v) using mole fractions. Implicit solvation of Li^+ was used since it has been proven to be a reliable approach for >1 M concentrations.[83]

Part III

Current work

Chapter 3

The role of anions in concentrated electrolytes for Li-S batteries

Abstract

HCEs show promise in enhancing Li-S battery performance by mitigating PS solubility. The role of the salt anion for the performance improvement(s) is however not well understood. Here a systematic characterisation using (concentrated) electrolytes based on three different salts: LiTFSI, LiTf, and LiTDI, in a common DOL:DME solvent mixture is reported for a wide range of physicochemical and electrochemical properties: ionic conductivity, density, viscosity, speciation, and PS solubility. While increased salt concentration in general improves Li-S battery performance, the role of the salt anion introduces complexity. The 2 m LiTDI-based electrolyte, with a slightly higher viscosity and lower PS solubility, outperforms the LiTFSI-based counterpart in terms of accessible reversible capacity. Conversely, the 2 m LiTf-based electrolyte exhibits subpar performance due to the formation of ionic aggregates that renders more free solvent and, therefore higher PS solubility, which, however can be improved by using a 5 m concentrated electrolyte. Hence, using electrolyte salt concentration as a rational design route demands an understanding of the local molecular structure, largely determined/affected by the choice of anion, as well as how it connects to the global properties and in the end improved Li-S battery performance.

3.1 Background

HCEs, also known as 'solvent-in-salt'[56] electrolytes and similar to 'polymer-in-salt'[87,88] electrolytes can be used to limit the solubility of PS.[45,89,90] In these electrolytes, the Li^+ cations in general coordinate more to the anions than to the solvent molecules, and simultaneously, there is a decrease in free solvent, both improving the performance of Li-S batteries.[91,92] Moreover, the increased concentration of Li^+ promotes a more homogeneous plating/stripping process and a robust anion-derived SEI that suppresses side reactions between the electrolyte and the lithium metal anode.[93] Overall, HCEs inhibit dendrite growth.[39] Most often, HCEs consist of conventional

lithium salts (LiTFSI, LiTDI, LiTf) dissolved in organic solvents, such as mixtures of DOL and DME.[94]

LiTFSI has been used at high concentrations in Li-S batteries by Shin et al., much due to its ability to suppress the solubility of LiPS through the common ion effect.[48] Subsequently, the concentration of this salt was increased even further, up to 7 mol/litre of solvent, resulting in impressive performance with over 800 mAh/g and close to 100% coulombic efficiency.[56] Equimolar mixtures of glymes with lithium salts such as LiTFSI and LiTf have also been investigated in Li-S batteries. The former, termed solvate ionic liquid, SIL, results in low solubility of polysulfides, while the latter, a concentrated electrolyte with high ionic association strength renders high PS solubility.[45,95] Another reason for the popularity of LiTFSI and LiTf for HCEs is their high thermal stabilities and compatibility with the ether solvents.[25,94] In particular LiTFSI is highly dissociated in DOL:DME, while LiTDI is a Hückel anion-based salt[57] that has weak interaction with polysulfides.[23,96]

Though HCE's have many advantages, many challenges still limit the application of HCEs. HCEs, apart from being expensive due to large amounts of salts, also have high viscosities and low ionic conductivities.[97] The high viscosity of HCEs can extend their wetting time compared to conventional electrolytes if a similar manufacturing process is used.[97] To improve the cyclability and overall performance of HCEs, a better understanding of physicochemical properties of these electrolytes is required.

Previous research has explored concentrated LiTFSI-based electrolytes ranging from 1 to 7 mol/litre[56] and LiTf-based ones up to 3 mol/litre, while for LiTDI-based electrolytes the salt concentration has been limited to 1 mol/litre.[98] In contrast, we here combine experimental and computational approaches to investigate electrolytes based on LiTFSI, LiTDI, and LiTf dissolved in a binary solvent mixture of DOL: DME (1:1, v/v) up to each and every system's maximum salt solubility. We aim to provide fundamental structural and mechanistic insights into the role of the lithium salt anion in different HCEs and less concentrated electrolytes. The physicochemical properties and electrochemical battery performance are rationalised using local structure analysis and speciation, including PS solubility.

3.2 Results and discussion

Initially, we prepared a series of electrolytes by dissolving appropriate amounts of LiTFSI, LiTf and LiTDI (Figure 3.1) in DOL:DME (1:1, v/v). Subsequently, we conducted a detailed analysis of the speciation ("free" anions, ion-pairs, and aggregates) in these electrolytes for various salt concentrations, with special emphasis on the role of the different anions/salts. Then findings were connected to the physicochemical properties and ionicities to further understand these properties, alongside S_8 and Li_2S_8 solubilities via both HPLC measurements and COSMO-RS modelling, affect Li-S battery performance.

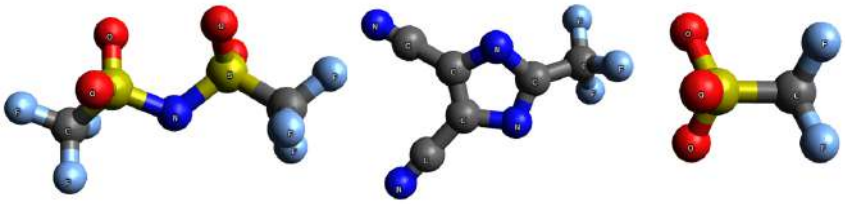

Figure 3.1: Chemical structures of the anions TFSI (bis(trifluoromethanesulfonyl)imide) (left), TDI (4,5-dicyano-2-(trifluoromethyl)imidazolide) (middle), and Tf (trifluoromethanesulfonate) (right).

3.2.1 Local structure and speciation

The electrochemical performance of an electrolyte depends on its physicochemical properties, such as local structure and speciation, ionic conductivity and viscosity. The local structure and speciation *i.e.,* "free" anions, ion-pairs, and aggregates.[51,99]

In HCEs, the interaction between the lithium cations and the anions leads to the formation of ion-pairs (solvent-separated or contact ion-pairs) and aggregates,[103] which can be semi-quantitatively determined by deconvolution of the electrolyte Raman spectra (Figure 3.2.

For all three electrolytes at standard 1 m concentrations, we observe a band of "free" anions at 739 cm^{-1} for LiTFSI (Figure 3.2a), at 2227 cm^{-1} (Figure 3.2b) and at 977 cm^{-1} (Figure A.5a) for LiTDI and at 757 cm^{-1} (Figure 3.2c) and at 1032 cm^{-1} (Figure A.5b) for LiTf.[51] The presence of these "free" anions can be rationalised using Debye-Hückel theory, which explains that as the electrostatic interactions decrease, the concentration of "free" ions increases.[103] As the salt concentration increases, we observe band splitting and a gradual shift towards higher frequencies (Figure 3.2a,b,c), signatures of an increase in ion-pairs and aggregates and a decrease in "free" anions in line with previous reports.[51,101–103]

These trends and hence the ionic association strength of the anions, depend on the charge delocalisation within the anion.[103] Anions can also be considered as Lewis bases with donor numbers (DNs).[25] A strong Lewis base interacts more strongly with a strong Lewis acid, such as a lithium-ion. In particular, for LiTFSI, the large concentration of "free" anions indicates higher ionic dissociation and hence more lithium ion-solvent coordination, that in turn leads to less free solvent present. This agrees with TFSI being a relatively weak Lewis base (DN = 5.4 kcal/mol) and interacts weakly with the lithium ions. LiTDI is in many ways intermediate between LiTFSI and LiTf, and we observe the presence of ion-pairs and aggregates in the 2 m LiTDI electrolyte.[104] For LiTf, less "free" anions indicate less ionic dissociation and hence less lithium ion-solvent interactions, leading to more "free" solvent as also seen in Figure 3.3. The Tf anion is a strong Lewis base (DN = 16.9 kcal/mol) and therefore interacts strongly with the lithium ions.[104]

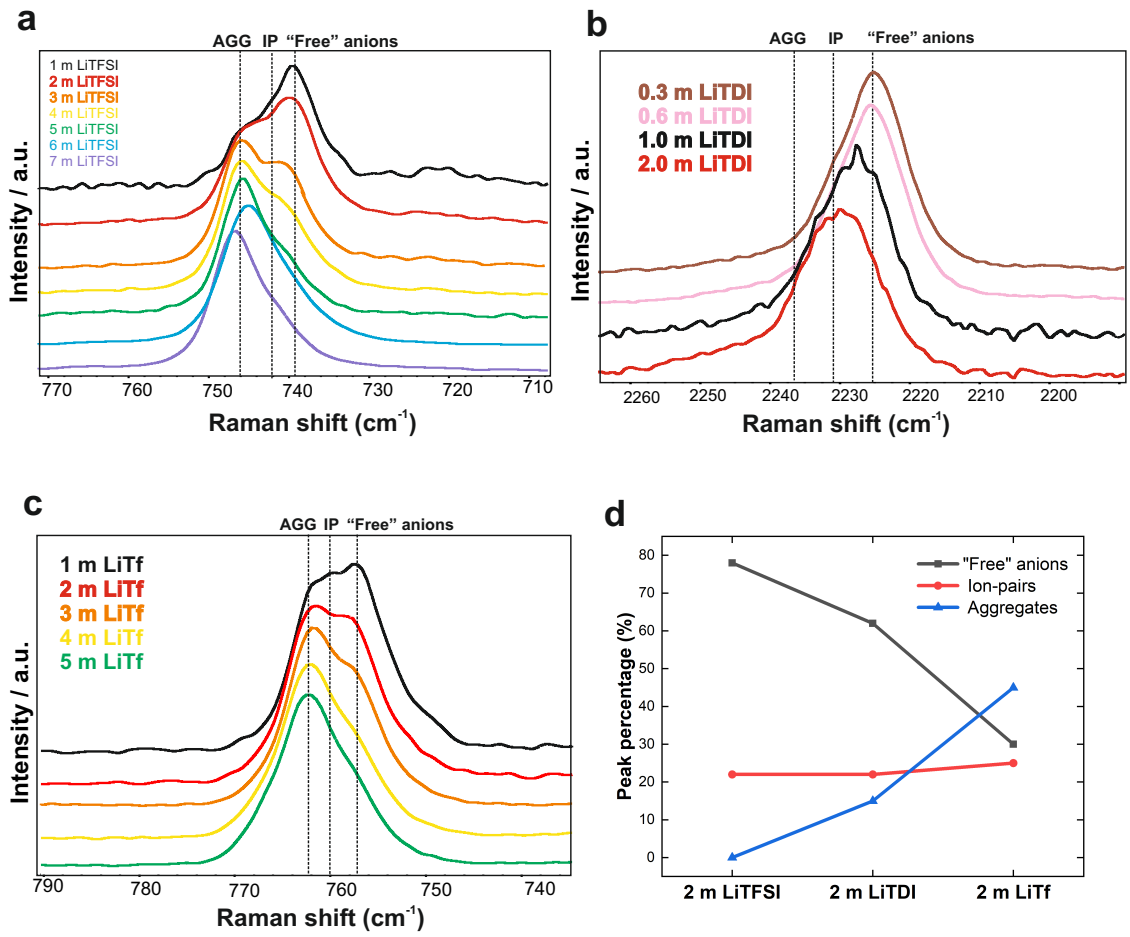

Figure 3.2: (a) Raman spectra in the ν_s(S-N-S) region for 1-7 m LiTFSI in DOL:DME (b) the ν_s (CN) bending region for 0.3-2.0 m LiTDI in DOL:DME (c) the $\delta_s(CF_3)$ bending region for 1-5 m LiTf, and (d) Comparison of the estimated amount "free" anions, ion-pairs, and aggregates for the 2 m LiTFSI, LiTDI and LiTf in DOL:DME (1:1, v/v) electrolytes.[65, 100–102]

3.2.2 Ion transport

The Li-S battery performance also depends on the ionic conductivity and viscosity, and in general, the former decreases and the latter increases as a function of salt concentration (Figure 3.4a).

For a common 2 m salt concentration, the trend in ionic conductivity is: LiTFSI > LiTDI > LiTf, which is similar to the trend for "free" anions. However, the viscosity is not inversely proportional to the ionic conductivity, as one might expect (Figure 3.4a); LiTFSI ≈ LiTDI > LiTf. The low ionic conductivity of the LiTf-based electrolyte can be explained by the extensive ionic association and the low viscosity can be rationalised by a large amount of free solvent[105] evident from the Raman spectra (Figure 3.3). As the salt concentration increases from 1 m to 3 m, the viscosity does not increase significantly (viscosity < 5 mPa.s). However, the

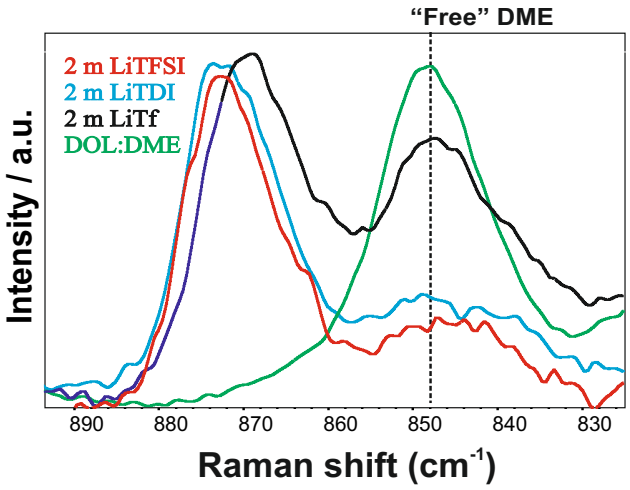

Figure 3.3: Comparison of spectra corresponding to the combined C-O stretching and CH_2 rocking vibrations of DME in the DOL:DME along with 2 m LiTFSI, LiTDI and LiTf in DOL:DME electrolytes.

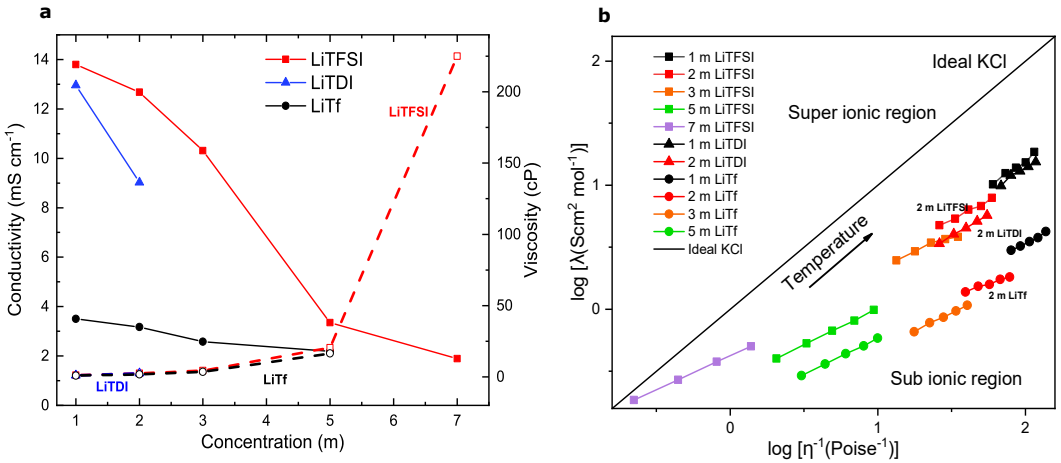

Figure 3.4: (a) Ionic conductivity and viscosity of the electrolytes at 30°C, filled symbols are conductivity and the open ones are viscosity (b) Walden plot from temperature-dependent molar conductivities and viscosities.

viscosity increases significantly at 5 m, to 16.4 mPa.s. For LiTFSI (1-7 m), the situation is quite different; the viscosity increases from 1.15 mPa.s to a vast 225 mPa.s, while the ionic conductivity decrease is much less pronounced (Figure 3.4a). Furthermore, to assess the ionicity, we analyse the Walden plot (Figure 3.4b) that

depicts the relation between transport properties, including the molar conductivity (λ) and the fluidity (η), the reciprocal of viscosity.[54,106]

Here, the observations at different temperatures (10-50 °C) for the same electrolyte family show that as the salt concentration increases, the ionicity decreases (Figure 3.4b). For the 2 m concentration electrolytes, the trend in ionicity is: LiTFSI > LiTDI > LiTf, which is similar to the trend for "free" anions and ionic conductivity. At very high salt concentrations, as for 7 m LiTFSI, the electrolyte approaches the superionic region, which also can be correlated with a report on high transference numbers (0.73) for this specific electrolyte.[56]

The ion transport mechanism in HCEs differs from that in conventional dilute electrolytes depending on the Li-coordination with surrounding ions. In dilute/conventional electrolytes, a vehicular ion-conduction mechanism prevails, i.e. the Li+ ion moves with its solvation shell and uncoordinated or "free" anions exhibit long lifetimes.[107,108] In HCEs, the Li^+ ion moves in concerted aggregated motions, hops, or exchanges its solvent shell, phenomena described as structural diffusion[53,54] or non-vehicular/exchange mechanisms[109], as for example reported to occur for sulfolane and acetonitrile-based HCEs.[93,110]

3.2.3 Electrochemical performance

The electrochemical performance tests using the different electrolytes did not comprise the 4-7 m LiTFSI electrolytes as these are already reported in the literature for the same solvent mixture (DOL:DME, 1:1, v/v).[48,56]

For all cells, during the first discharge, we observe a plateau at 2.3-2.4 V which is the elemental sulfur (S_8) accepting electrons to form long chain PS Li_2Sx (x=6-8), and subsequently a plateau at 2.1 V, which corresponds to the reduction of various PS Li_2Sx to Li_2S_2.[25,38]

The electrochemical performance is expected to improve at higher salt concentrations. In particular the LiTFSI-based electrolytes, going from 1 m to 3 m, the discharge capacity significantly increases from 220 mAh/g to 410 mAh/g (Figure 3.5a,b). For the LiTDI-based electrolytes, from 1 m to 2 m, the specific capacity increases from 300 mAh/g to 380 mAh/g (Figure 3.5c,d). For LiTf-based electrolytes, however, from 1 m to 3 m, we do not observe any significant increase in the specific capacity and even for the 5 m concentrated electrolyte, we observe a specific capacity of a mere 230 mAh/g (Figure 3.5e,f). This observation can indeed be correlated with the high concentration of "free" solvent and the low viscosity of these electrolytes, resulting in increased PS solubility.[96,111]

The coulombic efficiency (CE) improved with increased salt concentration (Figure A.6). The lower CEs, characterized by a decrease in discharge capacity and an increase in charge capacity, are attributed to the redox shuttle mechanism of PS. At lower electrolyte salt concentrations, the CE is overall notably low for the initial cycles but gradually improves, albeit with an inevitable decrease in capacity. In contrast, for higher salt concentrations, the CE remains above 80% from the initial cycles up to 50 cycles, which can be attributed to the lower Li_2S_8 solubility, indicating that the solid Li_2S_x remains in the composite cathode and undergoes a reversible redox reaction.[45]

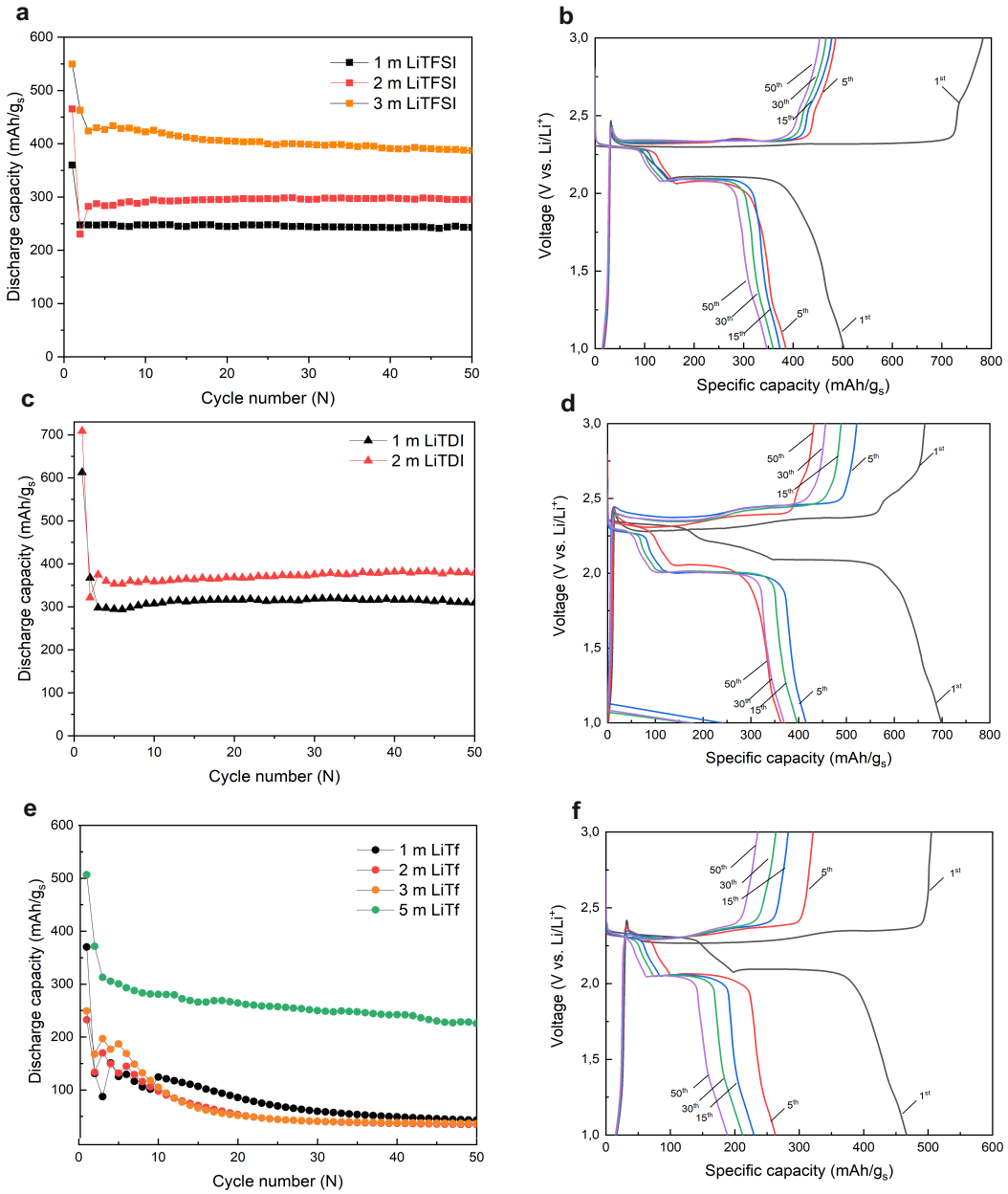

Figure 3.5: Cycling behaviour at C/10 (1st cycle C/30) for LiTFSI, LiTDI and LiTf in DOL:DME (1:1,v/v) (a, c, e) discharge capacity of LiTFSI (1-3 m), LiTDI (1-2 m) and LiTf (1-5 m) (b, d, f) the discharge-charge voltage profiles for the 3 m LiTFSI, 2 m LiTDI and 5 m LiTf.

For the comparative analysis of the electrolytes at the 2 m salt concentration, the discharge capacities follow: LiTDI > LiTFSI >> LiTf (Figure 3.6a).

The initial specific discharge capacity for LiTDI, LiTFSI, and LiTf is 710 mAh/g, 465 mAh/g, and 230 mAh/g, respectively (Figure 3.6b). Note that for LiTFSI and

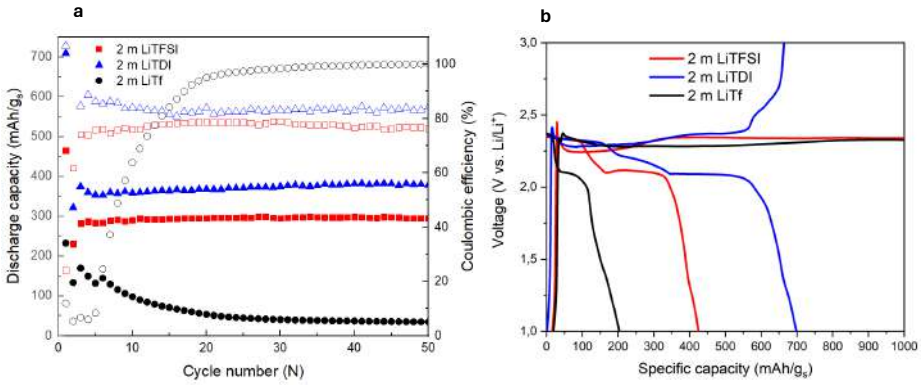

Figure 3.6: (a) Comparison of discharge capacity of 2 m LiTFSI, LiTDI, and LiTf (b) discharge-charge profiles at cycle 1 for the 2 m LiTFSI, LiTDI and LiTf-based electrolytes.

LiTf, the initial charge capacity may be significantly higher than the discharge capacity, as compared to the LiTDI-based electrolytes. The overcharging observed for LiTFSI and LiTf are possibly due to the lithium PS shuttle mechanism and side reactions of the lithium anode, which prevents the full discharge capacity from being regained on charging. The CEs are similar for the LiTFSI and LiTDI-based electrolytes, around 80%, while it is quite low for the LiTf-based electrolytes.

Overall, we observe the best electrochemical performance at 2 m concentration for the LiTDI-based electrolyte, which may at first look appear surprisingly as the LiTFSI-based electrolyte has more "free" anions, less free solvent, and higher ionic conductivity, but the slightly higher viscosity of LiTDI alongside with its lower PS solubility, is decisive.

3.2.4 Elemental S_8 and PS solubility

To actually examine the solubility of PS and sulfur, we use HPLC-DAD (2.2.2) and Li_2S_8 using COSMO-RS modelling[112] (Figure 3.7 and Table A.2). The experimental S_8 solubility trend follows: LiTf > LiTDI > LiTFSI, which thus explains the poor performance of the LiTf-based electrolytes, but it does not explain the better performance of the LiTDI-based electrolytes.

The solubility of LiPS, in any electrolyte, depends on several factors, such as the cation-anion interaction strength and the solvent molecular structures.[113] Electrolytes with stronger cation-anion interactions are expected to have higher LiPS solubility as the Li^+ cation interacts strongly also with the PS anion, and in e.g. the LiTf-based electrolytes, there is also abundant free solvent, due to the solvation of Li^+ by Tf anions, which in addition, as it is stronger or comparable to the Li^+-PS interaction, leads to Li_2S_x dissociation and high PS solubility.[95] Between the LiTDI and LiTFSI based electrolytes, though the former has slightly more ion-pairs than the latter, the modelling suggests Li_2S_8 to be more soluble in the latter (Table A.2). This is consistent with previous studies attributing lower Li_2S_8 solubility in LiTDI

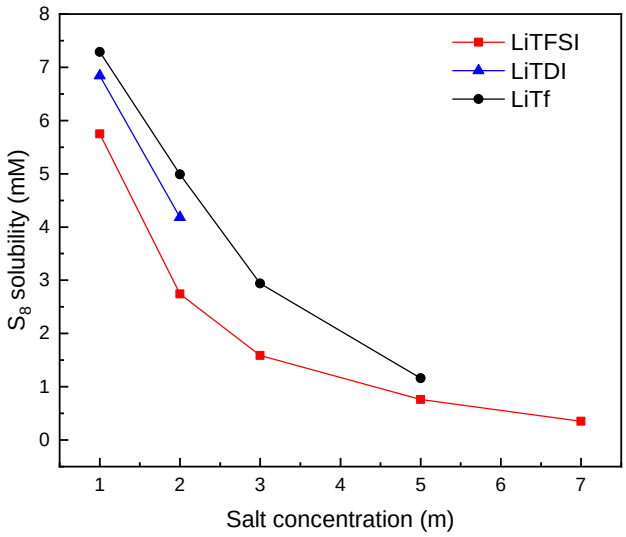

Figure 3.7: Solubility of S_8 in various electrolytes using HPLC-DAD (219 nm).

due to the large anion size as well as different solvation of LiTDI with Li_2S_8 forming dimers, as compared to monomers or higher order polysulfides in the case of LiTFSI-based electrolytes.[23,96]

3.3 Concluding remarks

Increasing the salt concentration in the electrolytes show promise for improving the performance of Li-S batteries. For our three electrolyte families based on LiTFSI, LiTDI or LiTf salts, the increase in ion-pairs and aggregates, the higher viscosities, and lower ionic conductivities at higher salt concentrations result in reduced PS solubility. Comparing the 2 m electrolytes, the trends in "free" anions and ionic conductivity aligns, but the viscosity trend does not. The lower viscosity observed for the LiTf-based electrolytes, combined with / originating from the presence of more free solvent, likely contributes to their comparatively poorer performance as the PS solubility increase, while in contrast the LiTDI-based electrolytes have a large capacity (380 mAh/g), possibly due to their lower PS solubility and this both emphasizes the role of the anion for improving the performance and suggest potential for exploring similar electrolytes based on Hückel anions for Li-S battery application.

Chapter 4

Hückel anion based concentrated electrolytes for Li-S batteries

4.1 Background

Hückel salts are aromatic molecules with delocalized π-electrons. These salts were first proposed by M. Armand in 1995 and they continue to provide useful alternatives for better electrolytes.[114] In Chapter 3, we reported the improved capacity of LiTDI-based electrolytes compared to the widely used LiTFSI-based electrolytes. The improved capacity of LiTDI is attributed to their lower polysulfide (PS) solubility compared to LiTFSI. This is due to the difference in lithium solvation with the most soluble PS, Li_2S_8, forming Li_2S_4 dimers.[23,96]

The enhanced electrochemical performance of LiTDI-based electrolytes motivates us to explore other Hückel anion-based salts in the same family, which differ only in the length of the perfluorinated alkyl chain, such as LiPDI (n=2) and LiHDI (n=3). In this chapter, we envisage for the first time Hückel anion-based salts LiTDI, LiPDI, and LiHDI at various concentrations and study their local structure, ion transport, and electrochemical properties to introduce new electrolyte designs for Li-S batteries.

4.2 Results and discussion

Initially, we prepared a series of electrolytes based on LiTDI, LiPDI, and LiHDI (Figure 4.1) from 0.3-2 m in DOL:DME (1:1, v/v) solvent mixture. Subsequently, we analysed the local structure of the electrolytes as a function of salt concentration using Raman and FTIR spectroscopy. Furthermore, these structures were correlated with ion transport properties and electrochemical performance. The electrochemical performance depends on PS solubility in the electrolytes. The Li_2S_8 polysulfide solubility was determined using the COSMO-RS combined with the multiple linear regression model.

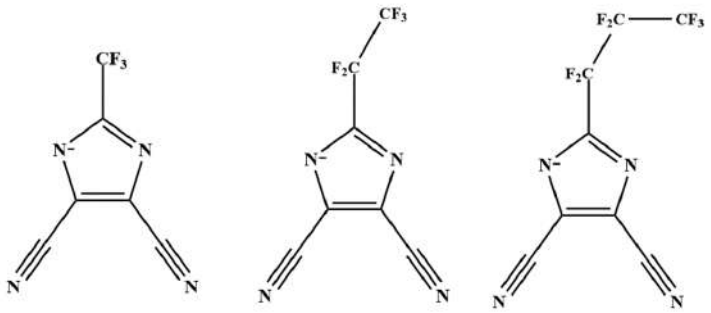

Figure 4.1: Chemical structures of LiTDI (left), LiPDI (middle) and LiHDI (right)

4.2.1 Local structure and speciation

The Raman and FTIR spectra of Hückel anion-based concentrated electrolytes provide insights into the coordination environment of lithium ions and the nature of ion-solvent and ion-ion interactions.[115] Previous studies from the Wieczorek group reported several crystalline solvate structures and Raman spectra of LiTDI with dimethyl ethers of glymes.[65] These spectra provide information for comparing the ionic association of salts (LiTDI, LiPDI, and LiHDI) in DOL:DME solvents since DME molecules are more actively involved in the Li^+-solvation process than DOL.[96] The spectra, shown in Figure 4.2, represent peaks for various concentrations (0.3 m, 0.6 m, 1.0 m and 2 m) of LiPDI in a DOL:DME solvent mixture. It consists of three main bands (Figure 4.2), that serve as crucial probes for the analysis of ionic association: CN triple bond stretching (ν_{CN}, 2225-2235 cm^{-1}), imidazole ring stretching (ν_{CN-Im}, 1300-1320 cm^{-1}), and NCN ring deformation (δ_{NCN}, 943-977 cm^{-1}).[65,116]

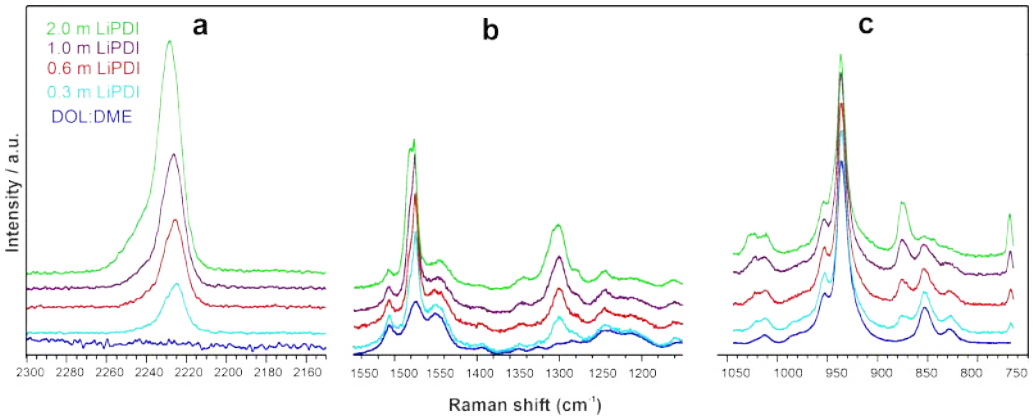

Figure 4.2: Raman spectra of 0.3-2m LiPDI in spectral ranges corresponding to a) ν_{CN}, b) ν_{CN-Im} and c) δ_{NCN}

The intensity of the peak in the 2225-2235 cm^{-1} increases with salt concentrations, indicating an increase in the number of PDI anions interacting with the lithium ions. The peak at 1300-1320 cm^{-1} and 943-977 cm^{-1} shifts to a higher wavenumber, and its intensity increases with the salt concentration. This observation suggests that there are changes in the local coordination environment and the nature of ion-solvent interactions. In particular, the increase in peak intensity with

salt concentration suggests that the electrolyte environment becomes more structured, and there is a higher degree of coordination between the ions and solvent molecules.

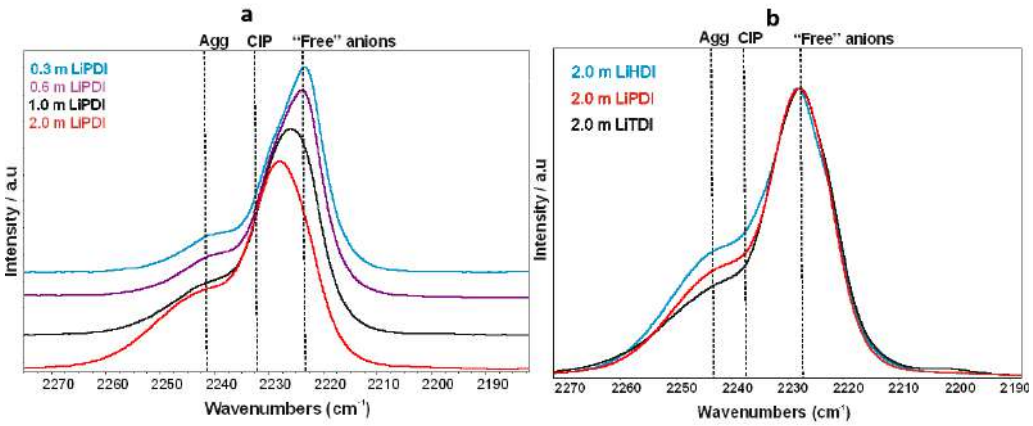

Figure 4.3: a) FTIR spectra of LiPDI (0.3-2 m salt concentration) in a solvent mixture of DOL:DME b) Comparison of νCN peak for 2 m LiTDI, LiPDI and LiHDI.

The FTIR spectra provide complementary insights into the coordination environment and speciation of Hückel anion-based electrolytes. The peak at 2225 cm^{-1} for 0.3 m salt shifts to higher wavenumbers and is accompanied by a shoulder at 2245 cm^{-1}. Deconvoluted CN stretching bands for LiPDI in DOL:DME (Figure 4.3a) reveal three distinct peaks for "free" anions (2223 cm^{-1}), contact ion-pairs (2230 cm^{-1}), and aggregates (2241 cm^{-1}). The percentage of "free" anions decreases with increasing salt concentration, while ion-pairs remain between 40-60%, and the percentage of aggregates (triplets or dimers) significantly increases. Higher concentrations of dimers also contribute to the poor ionic conductivity as they are less mobile under an electric field.[117] The deconvolution results of the ν_{CN} peak (Figure 4.3b) show that the amount of aggregates is lowest for LiTDI among the three salts, while the amount of "free" anions is slightly higher for LiTDI than for LiPDI and LiHDI. The highest degree of free anions in LiHDI-based electrolytes is possibly due to its larger anion size and lower mobility.[96] The spectral changes between 820-900 cm^{-1} corresponding to CH_2 rocking and C-O-C stretching vibrations of DME (Figure 4.4) suggest that the amount of free solvent in the electrolyte decreases as the salt concentration increases. A prominent band at approximately 870 cm^{-1} (breathing mode) corresponds to the glyme-lithium salt complex. The band intensity increases at the expense of the band at 850 cm^{-1}, which is a characteristic of free solvent.[118–120]

In general, FTIR spectra confirm the trends observed in Raman spectroscopy, emphasizing the importance of salt concentration and the choice of lithium salt on the coordination environment in Hückel anion-based electrolytes. At higher concentrations, the increase in interaction between lithium ions and anions leads to enhanced structural stability and reduced ion transport.

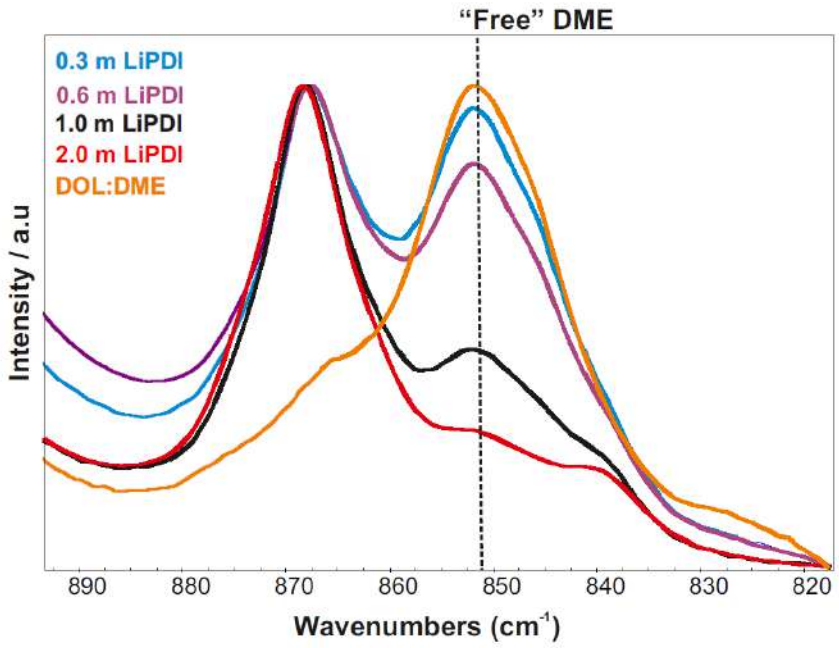

Figure 4.4: Comparison of spectra corresponding to the combined C-O stretching and CH_2 rocking vibrations of DME in the DOL:DME along with 0.3-2 m LiPDI.

4.2.2 Ion transport

To further understand the ion transport of Hückel anion-based electrolytes, we examined the ionic conductivity and viscosity of 1 m and 2 m concentrations of LiTDI, LiPDI, and LiHDI from 0-50 °C (Figure 4.5). The ionic conductivity of the electrolytes depends on several factors such as the ionic association strength, the type of lithium salt anion, and salt concentration.[121] The ionic conductivity for 1 m and 2 m LiTDI, LiPDI, and LiHDI increases, and viscosity decreases with temperature. The conductivity values are lower for 2 m compared to the 1 m salt concentration due to increased viscosity and ion pairing in 2 m. The LiTDI-based electrolyte exhibits the highest conductivity and lowest viscosity, followed by LiPDI and LiHDI in the temperature range investigated in this work. The differences in ionic conductivity of different salts are slightly more pronounced at 2 m salt concentration and correlate well with viscosity results. The ionic conductivity trend agrees with the previous work on similar electrolytes which showed that LiTDI has slightly higher ionic conductivity compared to LiPDI in triglyme solvents.[121]

4.2.3 Electrochemical performance

Due to the higher amount of free solvent at 0.3 and 0.6 m salt concentrations, the electrochemical performance of the Hückel salt-based electrolytes for Li-S batteries was performed for 1 m and 2 m lithium salt concentrations. We reported the discharge capacity of Li-S batteries for the first 50 cycles in Chapter 3 (Figure 3.5) for the LiTDI in DOL:DME electrolytes. The LiTDI-based electrolytes had outperformed LiTFSI-based electrolytes in their capacity and coulombic efficiency. In this work our aim was to check if the LiPDI and LiHDI-based electrolytes behaved

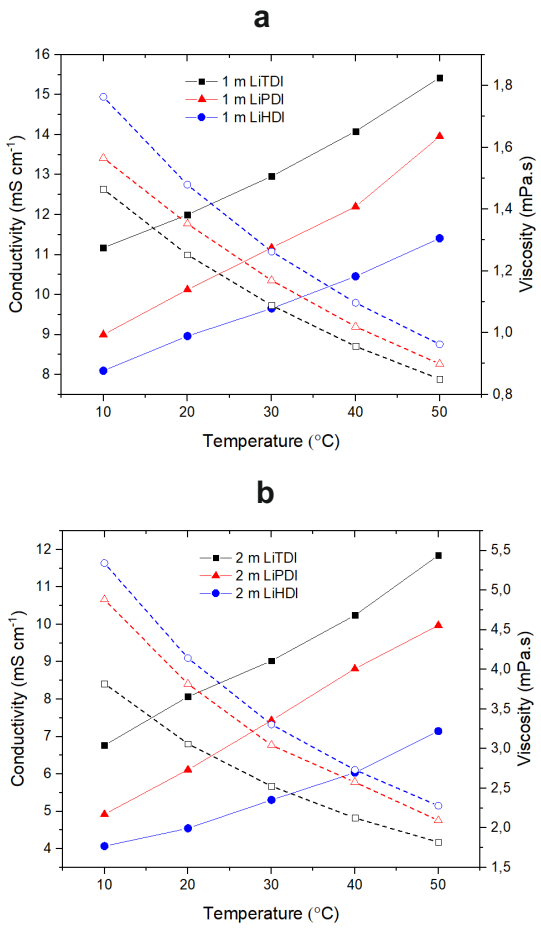

Figure 4.5: Ionic conductivity and viscosity of a) 1 m and b) 2 m LiTDI, LiPDI and LiHDI: the solid line represents ionic conductivity and the dashed line represents viscosity.

similar to LiTDI.

The discharge capacity of electrolytes based on 2 m lithium salt was higher than the 1 m due to low PS solubilities. Here, we compare the first charge-discharge behaviour of Li-S using 2 m LiTDI, LiPDI, and LiHDI (Figure 4.6). The initial capacities of LiPDI and LiHDI were only slightly lower than that of LiTDI, with no significant overpotential observed at 2 m salt concentration. An improvement in electrochemical performance was observed when the concentration increases from 1 m to 2 m and we compare the cycling performance and coulombic efficiency for the first 10 cycles (Figure 4.7a). The discharge capacities remained relatively consistent for all electrolytes, ranging from 350 to 400 mAh/g. The coulombic efficiency improved significantly with an increase in concentration from 1 m to 2 m (Figure A.6) but remained between 60-85%. The addition of $LiNO_3$ additive further enhances anode stability, resulting in nearly 100% coulombic efficiency (Figure 4.7b), suggesting that both LiPDI and LiHDI are good candidates for Li-S batteries.

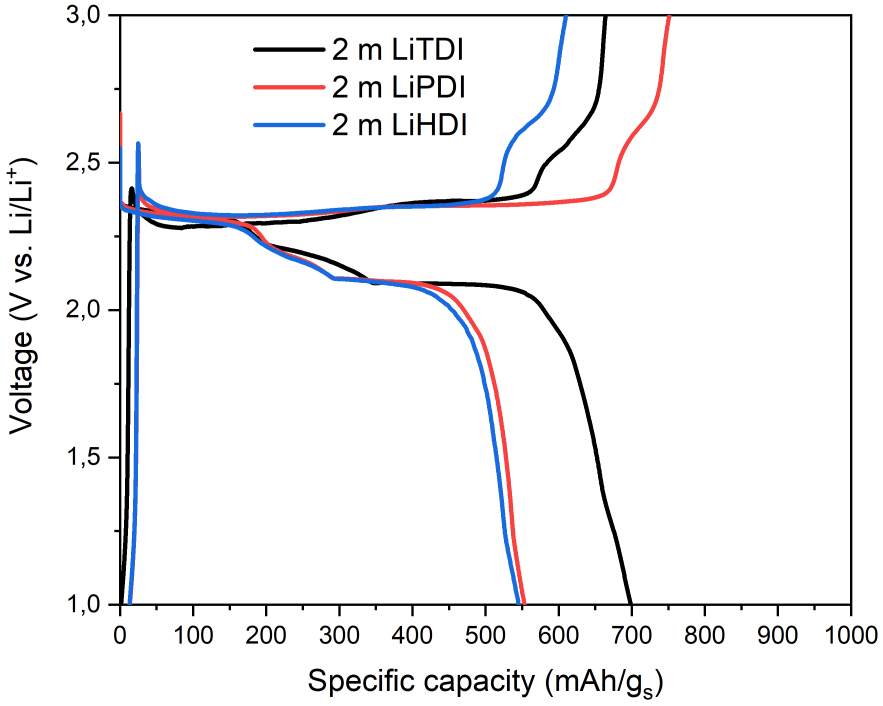

Figure 4.6: Comparison of first charge-discharge capacity of 2m LiTDI, LiPDI and LiHDI.

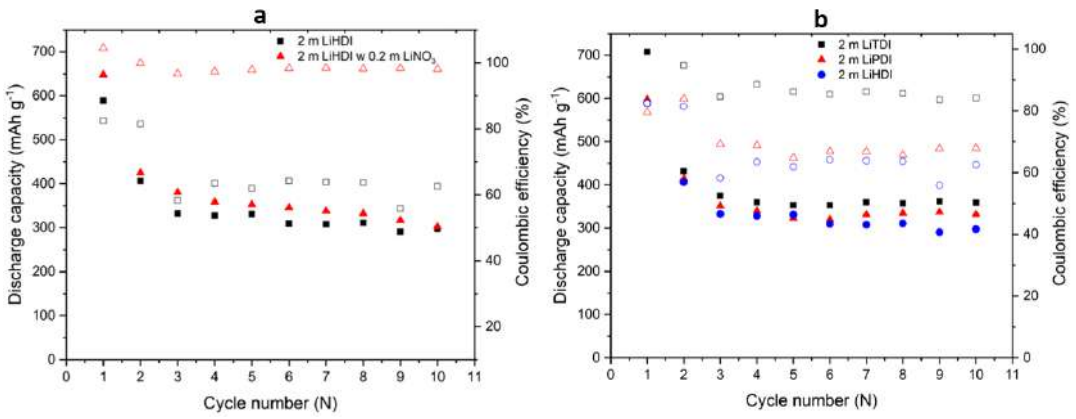

Figure 4.7: Cycling behavior at C/10 for 2 m LiTDI, LiPDI, and LiHDI in DOL:DME solvent mixture. a) Cycle 1 with C-rate = C/30 b) Discharge capacity and coulombic efficiency of 2 m LiTDI, LiPDI, and LiHDI for the first 10 cycles c) Discharge capacity and coulombic efficiency of LiHDI for the first 10 cycles after the addition of 0.2 m $LiNO_3$.

4.2.4 Polysulfide solubility and modelling

Low PS solubility is an important parameter for enhanced Li-S battery performance, and here, we evaluate the Li_2S_8 solubility of LiTDI, LiPDI and LiHDI electrolytes

using COSMO-RS combined with a supervised machine learning approach. This approach is explained in detail in Chapter 5.

Table 4.1: Predicted Li_2S_8 solubility of LiTDI, LiPDI, and LiHDI in DOL:DME.

Electrolytes	**Li_2S_8 solubility log10[s]**
1 m LiTDI in DOL:DME	2.4
2 m LiTDI in DOL:DME	2.1
1 m LiPDI in DOL:DME	2.3
2 m LiPDI in DOL:DME	2
1 m LiHDI in DOL:DME	2.3
1 m LiHDI in DOL:DME	1.9

The table lists the Li_2S_8 solubility values, expressed as $\log_{10}[s]$, for 1 m and 2 m concentrations of LiTDI, LiPDI, and LiHDI in DOL:DME solvent mixture. For all three electrolytes, increasing the salt concentration from 1 m to 2 m decreases the Li_2S_8 solubility. The solubility of Li_2S_8 also decreases as the chain length of salt increases from LiTDI to LiHDI. This indicates that LiHDI may have lower PS solubility due to the larger anion size and reduced mobility due to higher viscosity.

4.3 Conclusions and outlook

In summary, we prepared and characterised a series of concentrated electrolytes based on Hückel anion salts with different alkyl chains for Li-S batteries. Raman and FTIR spectroscopy provided valuable insights into the local structure and the local structure correlates with ion transport properties and electrochemical performance. The increase in ion-pairs and aggregates, less free solvent and the increase in viscosity improved the capacity at 2 m salt concentration. The LiTDI, LiPDI and LiHDI-based electrolytes showed similar electrochemical performance, though the Li_2S_8 decreases as the alkyl chain length increases from LiTDI to LiHDI. The addition of $LiNO_3$, additive, further improved the coulombic efficiency, making them strong candidates for future Li-S batteries.

To further explore the PS solubility and diffusion mechanism in Hückel anion salts, *operando* Raman studies are performed as described in Chapter 6.

Chapter 5

Machine learning approaches for PS solubility prediction

5.1 Background

In Chapter 1, we discussed that one of the major challenges in Li-S batteries is the dissolution of PSs. This issue arises when elemental sulfur in the carbon-sulfur cathode dissolves into the electrolyte during Li-S battery operation and converts into various PSs. Long chain PSs, such as Li_2S_8, are more soluble in the electrolyte compared to shorter chain PSs.[122,123] Predicting and controlling the concentration of these PSs in the electrolyte remains a significant unresolved problem, and there are several attempts under development.[17,124] It is often very time-consuming to prepare LiPS based on different stoichiometries and analyse them using IR, UV spectroscopy, and other experimental techniques.[113] The COSMO-RS approach is well-suited for assessing PS solubility in electrolytes, as it provides multiple molecular descriptors with physical significance related to molecular interactions. Quantitative structure-activity/property relationship (QSAR/QSPR) involves combining experimental data and computed molecular descriptors to explain interactions and predict the activity or properties of chemical compounds based on their molecular structures.

In the current work, we describe a method that combines different supervised machine-learning approaches with COSMO-RS descriptors to build a regression model for PS solubility. We use this model to predict the Li_2S_8 concentration in Hückel anion-based electrolytes.

5.2 Results and discussion

The method used to predict the Li_2S_8 solubility is briefly explained in Figure 5.1. Initially, the molecular structures were built and optimised as described in Section 2.6. Using COSMO-RS, we obtained the σ-potential, $\mu(\sigma)$ or molecular descriptors of electrolytes at different salt concentrations. The experimental Li_2S_8 solubility values for 12 electrolytes were used to create a dataset, and the corresponding molecular descriptors were calculated from COSMO-RS. We then screened 127 potential combinations of these descriptors and statistically assessed the models using

the correlation coefficient (R^2). The coefficients with the least mean squared errors were used to predict the Li_2S_8 solubility of the Hückel anion-based electrolytes.

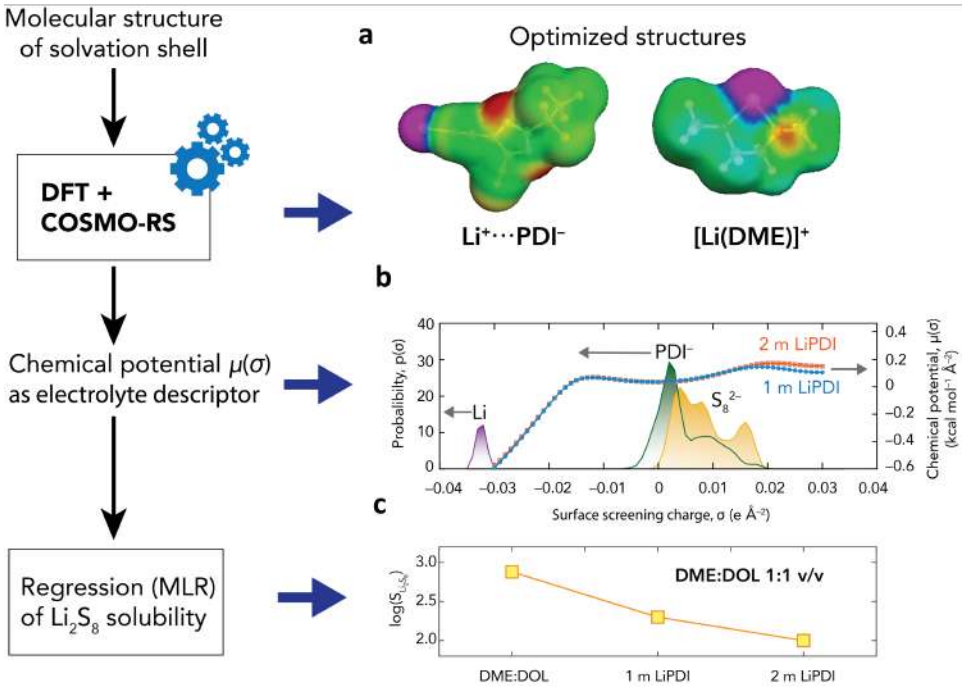

Figure 5.1: Workflow for COSMO-RS to obtain molecular descriptors followed by PS solubility for the Hückel salt-based electrolytes.

5.2.1 Chemical potential as a molecular descriptor

For developing the QSPR/QSAR model, the most useful molecular descriptor, the σ-potential ($\mu(\sigma)$) of the electrolytes was obtained from the COSMO-RS model. These descriptors were displayed as a sigma profile, that provides the probability ($p(\sigma)$) of finding a molecular surface segment with a screening charge σ on the surface of a molecule. The computed σ-potentials contained 61 data points ranging between $\pm 0.03 e Å^{-2}$.

From the Figure 5.1b, the σ-potentials of the Hückel anion-based electrolytes were nearly identical between 0 and $\pm 0.02 e Å^{-2}$, which corresponded to the σ-profile of the S_8^{2-} anion. Consequently, the ability of the electrolyte to interact with Li^+ determined the Li_2S_8 solubility. The $\mu(\sigma)$ was a valuable descriptor for quantifying the ability of electrolytes to solubilise polysulfides.

Among the data points between $\pm 0.03 e Å^{-2}$, many data points were similar to each other, leading to the reduction of the $\mu(\sigma)$ descriptors to 7 data points, *i.e.*, $\sigma = \pm 0.03$, ± 0.02, ± 0.01, and $0.0\, e Å^{-2}$.

5.2.2 Data collection

To predict the Li_2S_8 solubility for new electrolyte systems, we created a dataset with known Li_2S_8 solubilities based on previous experiments.[23,111,125] The dataset

Table 5.1: Descriptor values and Li_2S_8 solubility-experimental and predicted.

Solvent	$\mu(-0.02)$	$\mu(0.01)$	Exp $\log_{10}(s)$	Pred $log_{10}(s)$
DOL:DME, 1:1 (v:v)[113]	-0.147	0.077	2.88	2.92
1 m LiTFSI DOL:DME[23]	-0.109	0.079	2.70	2.40
THF[113]	-0.285	0.087	3.00	2.91
1 m LiTFSI $G4_{n=3}$[126]	-0.169	0.081	2.88	2.65
$[Li(THF)_2]TFSI \times 2$ THF[125, 127]	-0.143	0.086	2.24	1.90
$[Li(G4_{n=5})_1]$BETI[111]	0.105	0.081	0.30	0.50
$[Li(G2)_{4/3}]$TFSI[125, 127]	0.077	0.082	0.90	0.61
$[Li(G4_{n=5})_1]$TFSI[125, 127]	0.089	0.079	0.90	0.85
$[Li(G3_{n=4})_1]$TFSI[125, 127]	0.086	0.081	0.60	0.65
$[Li(G3_{n=3})_1]$OTf[111]	-0.159	0.077	3.11	3.01
$[Li(G1)_1]TFSI_xG1$[125, 127]	-0.136	0.086	1.40	1.85

includes 12 electrolytes containing binary and ternary solvent mixtures and various Li salts. The experimental Li_2S_8 solubility values were collected from previous reports (Table 5.1).

5.2.3 Regression model development and validation

Using one to seven $\mu(\sigma)$-descriptors ($\sigma = \pm 0.03$, ± 0.02, ± 0.01, and $0.0\,e\text{Å}^{-2}$), we screened 127 potential combinations of the descriptors to generate MLR-X models of increasing complexity X: $X = 1$–7; specifically, $X = 1:7$ combinations, $X = 2:21$, $X = 3:35$, $X = 4:35$, $X = 5:21$, $X = 6:7$, and $X = 7:1$.[112] Each MLR regression model using a different complexity X and a combination of $\mu(\sigma)$-descriptors was built and compared. The models were evaluated using mean squared error (MSE) and the correlation coefficient (R^2). A 70/30 split between training and test datasets was employed and this was repeated 30 times to ensure accuracy. Additionally, the difference between training and test MSE was used to assess model.

The MSE for the test datasets showed that MLR models with higher complexity initially decreased MSE, indicating a better fit. However, models with too many descriptors (MLR-6 and MLR-7) exhibited overfitting, while simpler models (MLR-1 and MLR-3) were underfitted. We found that the optimal model was MLR-2, as it balanced bias and variance effectively. The coefficients for these descriptors were determined, and the linear Equation 5.1 was obtained. The Equation 5.1 used for predicting the Li_2S_8 solubility is:

$$\log_{10}(s_{\text{predicted}}) = 7.84 \cdot \mu(-0.02) - 109.25 \cdot \mu(0.01) + 10.17 \tag{5.1}$$

Using the Equation 5.1 and the chemical potential values at $\mu(-0.02)$ and $\mu(0.01)$ the solubility of Li_2S_8 was calculated for the Hückel anion based electrolytes. (Chapter 4, Table 4.1).

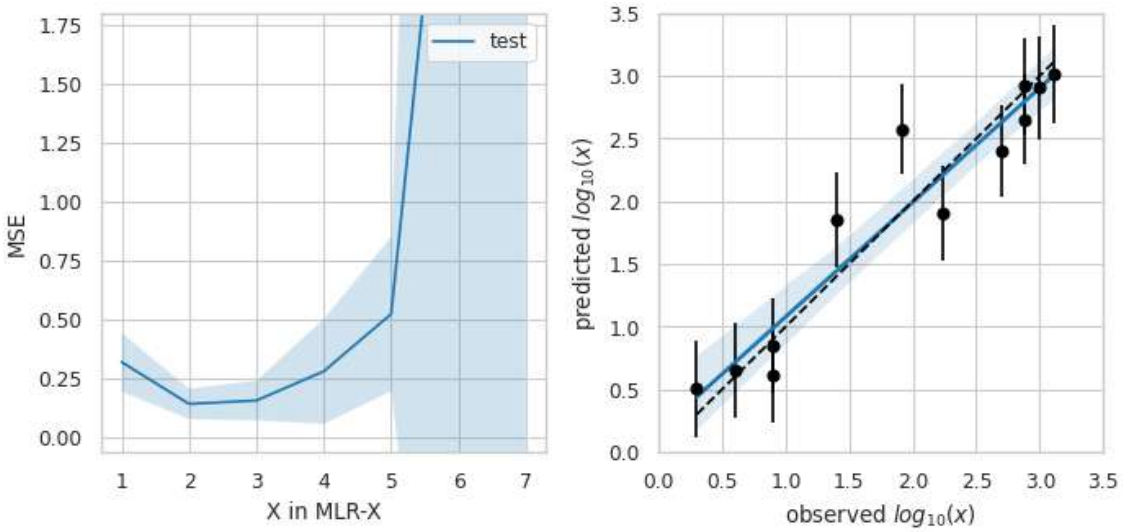

Figure 5.2: Learning curves and predicted Li_2S_8 solubility using linear regression MLR-2

5.2.4 Multiple linear regression model building

The open-source Scikit-learn toolkit (v0.22.1) for the Python programming language was utilised to implement supervised machine learning methods for model building.[128] A QSAR/QSPR model was developed using an ordinary least squares approach within the MLR technique to make predictions. Ordinary least squares regression is a widely used method for estimating the coefficients of linear regression equations, which describes the relationship between one or more independent quantitative variables and a dependent variable. This method enables the correlation of the computed $\mu(\sigma)$ of the COSMO-RS with the $\log_{10}$ of the experimental Li_2S_8 solubility s (in mM).

We tested 127 MLR regression models, each with unique complexity X and sets of molecular descriptors were constructed and compared. The models were validated using a cross-validation approach across 20 randomly selected datasets. The dataset was divided into training and test sets in a 70/30 ratio. The p-value analysis was conducted using the Python module statsmodels (v0.11.0).[112] The fitted models were statistically assessed using the correlation coefficient (R^2) and the corresponding mean-square error as described in Equation 5.2. This equation calculates the mean squared error between the calculated and experimental solubility values:

$$\mathrm{MSE} = \frac{1}{N}\sum_{i=1}^{N}\left(\log_{10}(s_{\mathrm{calc}}) - \log_{10}(s_{\mathrm{exp}})\right)^2 \tag{5.2}$$

In Equation 5.2, MSE is the difference between the predicted (calculated) and experimental values. Here, N represents the total number of data points or observations. The variables s_{calc} and s_{exp} denote the solubility values calculated using and the experimentally measured solubility values, respectively. The base-10 logarithm function, $\log_{10}$, is applied to these solubility values to compare them on a logarithmic scale. The summation operator, $\sum_{i=1}^{N}$, sums the squared differences between

the logarithms of the predicted and experimental values for all N data points, and the average of these squared differences is the MSE.

5.3 Conclusions

Our study successfully shows that supervised machine learning, particularly MLR models with carefully selected descriptors, can effectively predict Li2S8 solubility in Hückel anion-based electrolytes. The optimal MLR model, utilising two descriptors, achieved high predictive accuracy with $R^2 = 0.91$. The predicted Li_2S_8 solubility values show excellent agreement with experimental data, validating the robustness of this approach. In summary, the MLR approaches hold the potential for predictive modelling of PS solubility, which is crucial for electrolyte design and optimisation for Li-S batteries.

Chapter 6

Insights to PS dissolution and diffusion by *operando* Raman spectroscopy

6.1 Background

In Li-S batteries, PSs inherently solvate in liquid electrolytes and thereby contribute to loss of/ unstable cathode capacity and short cell life-spans. Despite attempts to address this issue through various electrolyte formulations, challenges persist due to our incomplete understanding of PS dissolution and diffusion, particularly across different cell state-of-charge and electrolytes. In this study, we semi-quantify the impact of electrolyte salt concentration on the solubility and diffusion behaviour of PSs using *in situ/operando* Raman spectroscopy, assisted by modelling efforts – DFT + COSMO-RS, modelling shown viable in the past to address differently concentrated electrolytes.[112] Specifically, we have here chosen a family of Hückel anion-based lithium salts, which differ only in their perfluoroalkyl chain, dissolved in the standard solvent mixture of DOL:DME (1:1, v/v) to prepare 0.3-2 m electrolytes.

By Raman spectroscopy we determined the local structure and found that more ion-pairs and aggregates decrease the PS solubility and mobility in the more salt concentrated electrolytes, and this finding was further supported by COSMO-RS modelling. This chapter will contribute to the understanding of the intricate PS solvation in liquid electrolytes for future Li-S battery development.

6.2 Results and discussion

All Li-S cells using Hückel anion-based lithium salt (LiTDI/LiPDI/LiHDI) electrolytes were after assembling charged to stable open circuit voltages (OCVs); up to 2.4 V for LiTDI (1–2 m) and up to 3.0 V for LiPDI (0.3–2 m) and LiHDI (1–2 m).

6.2.1 Raman spectra at open circuit voltage

The Raman spectra of the electrolytes in the Li-S cells at OCV are quite comparable to the spectra of the pure electrolytes (Figure. 6.1). In the Li-S cells using 1 and

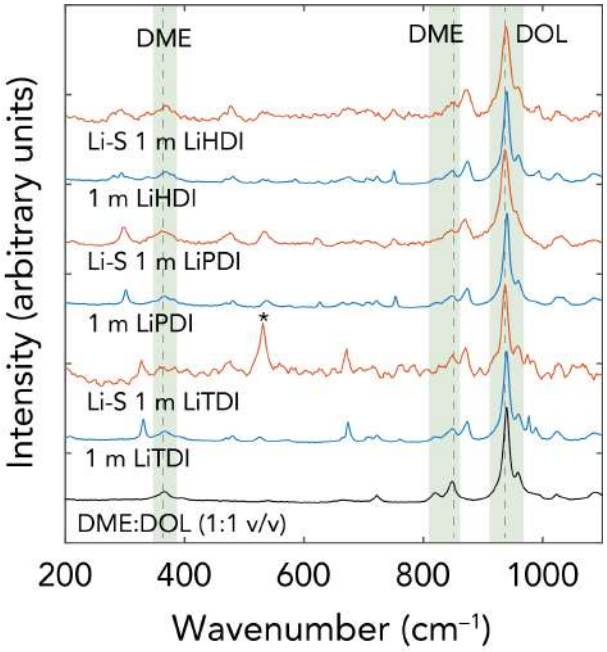

Figure 6.1: Comparison of Raman spectra of 1 m LiTDI, LiPDI and LiHDI in DOL:DME electrolytes in glass vials (blue spectra) and in Li-S cells at OCV (red spectra). The spectrum of the DOL:DME (1:1 v/v) solvent mixture is shown in black, and the asterisk marks the presence of the $S_3^{\bullet-}$ radical peak.

2 m LiTDI, the tri-sulfur $S_3^{\bullet-}$ radical[69,129] was detected at $\sim 530\,\mathrm{cm}^{-1}$ when at the high voltage plateau (2.4–2.3 V), despite the ambiguous detection of its parent long-chain S_6^{2-} species. Whereas the OCV of the Li-S cells using the LiPDI and LiHDI electrolytes is stable at 3.0 V, no Raman signals of sulfur species can be detected, at least at the Li anode side even though the sulfur is soluble in DOL:DME solvent[61] and can react with Li anode without any potential gradient. This indicates that the solubility and diffusion of dissolved sulfur is limited in the LiPDI and LiHDI electrolytes compared to LiTDI electrolytes, in agreement with our Li_2S_8 solubility calculations using COSMO-RS combined MLR model (Chapter 5). In all, this further confirms that among the Hückel salts LiTDI-based electrolytes have slightly higher S / PS solubility.

6.2.2 Raman spectra during galvanostatic cycling

During galvanostatic discharge of the Li-S cells using the 1–2 m LiTDI electrolytes (Figure. 6.2a,A.1), a set of new bands arises at ~ 400 and $\sim 441\,\mathrm{cm}^{-1}$ corresponding to S_6^{2-} and S_4^{2-},[68,69,129] respectively, when at the 2.4 V plateau and the 2.4–2.1 V slope. In addition, the $S_3^{\bullet-}$ radical band at $530\,\mathrm{cm}^{-1}$ continuously grew in intensity as function of depth-of-discharge, in agreement with a previous study using 1 m LiTFSI in DOL:DME (1:1 v/v).[129] Strong photoluminescence (PL) background (A.2) was

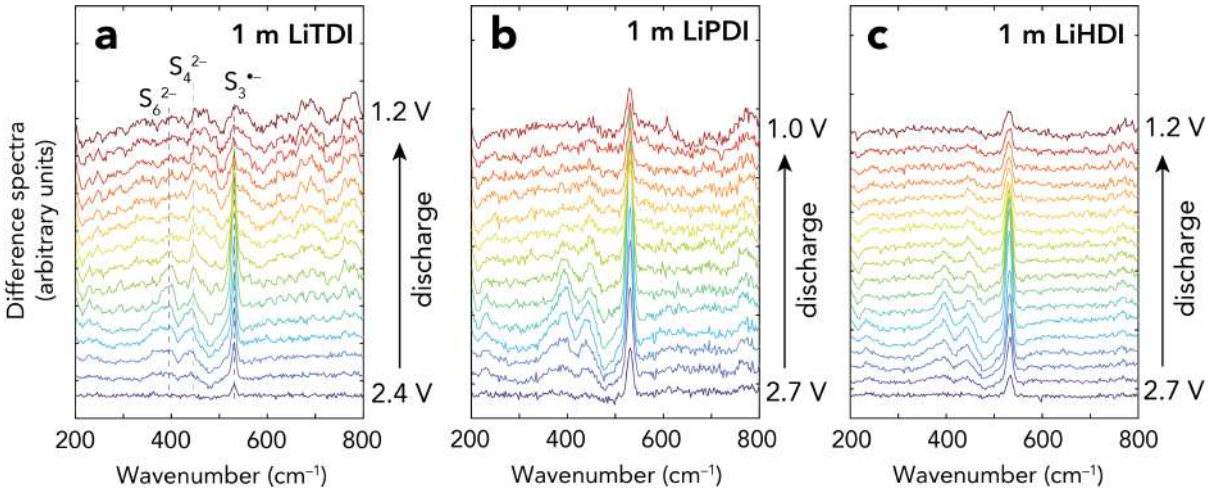

Figure 6.2: *Operando* Raman spectra of the first discharge of Li-S cells using the (a) 1 m LiTDI, (b) 1 m LiPDI, and (c) 1 m LiHDI electrolytes. Backgrounds were corrected for using polynomial functions, and the spectral response of the electrolytes at OCV was subtracted to enhance interpretation and readability.

present during the galvanostatic discharge, and overlaps with the Raman signals when entering the charge. Although electrochemical data for a few cycles in the *operando* Raman cell were comparable with those from the coin cell, we can only unambiguously analyse the Raman spectra from the first discharge cycle.

For the Li-S cells using 1–2 m LiPDI (Figure. 6.2b, A.2) and LiHDI (Figure. 6.2c, A.2), we observed the same collection of Raman bands of S_6^{2-} (400 cm^{-1}), S_4^{2-} (441 cm^{-1}) and $S_3^{\bullet-}$ (530 cm^{-1}), at the first discharge at 2.4 V plateau and 2.4–2.1 V slope. The 1 m LiPDI electrolyte spectra, less affected by PL (A.2) shows systematic growth and disappearance of PS species during cycling, in accordance with the literature.[69]

6.2.3 Concentration-dependent PS solubility and diffusion

To provide insight also on the electrolyte salt concentration-dependent PS solubility and diffusion, we analyzed the intensities of the S_6^{2-} (400 cm^{-1}), S_4^{2-} (441 cm^{-1}) and $S_3^{\bullet-}$ (530 cm^{-1})Raman bands. To minimise negative contributions of spectral noise, all intensity profiles (Figure. 6.3) were obtained by Gaussian fitting.

For the 1 m LiTDI electrolyte (Figure 6.3a), the intensity profiles reveal that the S_6^{2-} peaks appear before the $S_3^{\bullet-}$ radical peaks when coming to 2.3–2.1 V slope, even though the latter peak is present first during the OCV part. Subsequently, the populations of both these species decrease and finally disappear when the reduction progresses below 2 V, where the long-chain polysulfides are reduced to insoluble PSs: Li_2S and Li_2S_2. For the higher salt concentration (2 m LiTDI), S_6^{2-} and $S_3^{\bullet-}$ appear and reach their maxima in a manner similar to that of the 1 m LiTDI electrolyte. Notably, the maximum population of S_6^{2-} in 2 m appears slightly later than in 1 m, likely due to a slower reduction reaction during the initial 2.3 V plateau. While the concentration of S_6^{2-} detected at the Li anode side is comparable for the 1 m and 2 m LiTDI electrolytes, the $S_3^{\bullet-}$ appears in lower concentrations in the latter.

A similar behaviour is observed for the growth and the disappearance of S_6^{2-} and

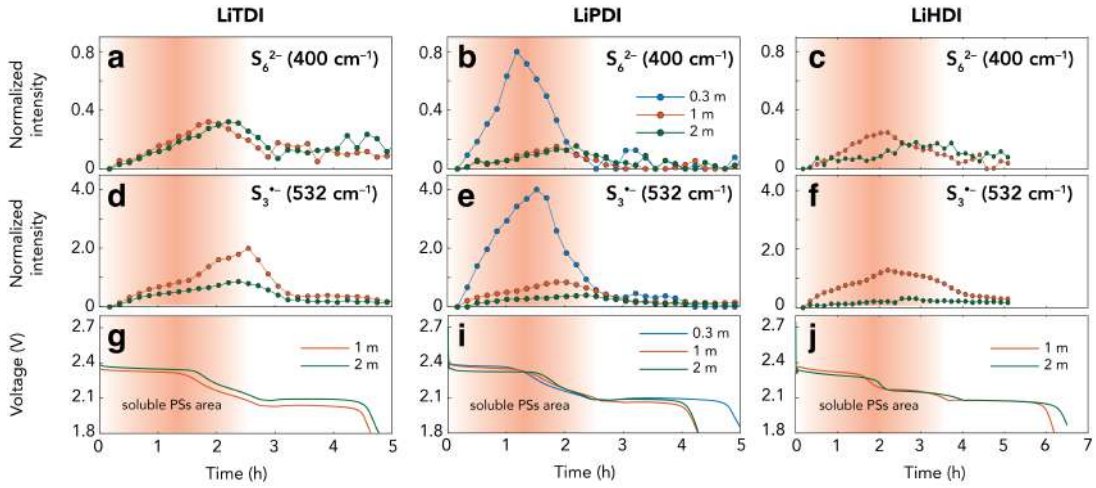

Figure 6.3: Gaussian intensity profiles of PS species produced during the first discharge of Li-S cells using variation of electrolytes concentrations. (a) 1–2 m LiTDI, (b) 0.3-2 m LiPDI and (c) 1-2 m LiHDI in DOL:DME. The intensities were normalised to the intensity of DOL at 950 cm^{-1} at OCV.

$S_3^{\bullet-}$ for both the 1 m and 2 m LiPDI electrolytes (Figure. 6.3c) as well as the 1 m and the 2 m LiHDI electrolytes (Figure. 6.3d), with only some minor differences. Specifically, the S_6^{2-} population is similar in the 1 m and 2 m LiPDI electrolytes, but is lower in the 2 m LiHDI electrolyte than in the 1 m LiHDI electrolyte. Additionally, the 2 m LiHDI electrolyte appears to slow down the mobility of S_6^{2-} as its population at the Li anode reaches its maximum ca. 60 minutes later than for the 1 m LiHDI. The voltage profile shows a relatively stable voltage plateau at 2.1 V associated with the reduction of Li_2S_4 to Li_2S_2 as well as the deeper $1e^-$ reduction to Li_2S.[38]

To clarify the behaviour of the S_6^{2-} PS at very low electrolyte salt concentrations and to isolate the impact of high salt concentration on PS solubility and diffusion, we conducted additional experiments with 0.3 m electrolytes of LiTDI, LiPDI, and LiHDI. The 0.3 m LiPDI electrolyte (Figure. 6.3b,e,i) revealed the populations of both S_6^{2-} and $S_3^{\bullet-}$ at the Li anode to be ca. four times higher than for the 1 m and 2 m electrolytes, suggesting that increased solubility and diffusion.

6.3 Conclusions and outlook

By *in situ/operando* Raman spectroscopy, we have successfully semi-quantified the impact of the LiTDI, LiPDI and LiHDI salt concentrations (0.3-2 m) on the solubility and diffusion behaviour of PSs in Li-S cells. The Raman spectra reveal fewer PS species at the Li metal anode side of the cell in the more concentrated electrolytes. This suggests either a decrease in PS solubility or a slower PS migration. Additionally, our COSMO-RS modelling supports that the PS solubility decreases moving from the 1 m to the 2 m electrolytes. Our study thus, contributes to the understanding of the intricate PS solvation in liquid electrolytes for future Li-S battery development.

Further studies could be undertaken to directly compare these Hückel salts with the more conventional X m LiTFSI electrolytes to provide valuable insights into the relative performance and efficiency of these electrolytes in Li-S batteries. Additionally, investigating the concentration of PS species present at the sulfur cathode side would be crucial for a comprehensive understanding of the electrolyte-sulfur interactions, paving the way to improve strategies to manage PS shuttling and thereby enhance overall Li-S cell performance.

Chapter 7

Summary and outlook

Enhancing the performance of Li-S batteries is a critical area of research, as in principle, the high energy density and cost-effectiveness of these batteries may offer significant advantages over conventional lithium-ion batteries. One promising approach to improve Li-S battery performance involves using HCEs to mitigate polysulfide solubility, which is a major challenge for the stability and efficiency of these batteries. In this thesis, we explored different lithium salts for Li-S batteries. In particular, we investigated LiTFSI, LiTf, LiTDI, LiPDI, and LiHDI, at various concentrations in a DOL:DME solvent mixture. The characteristic local coordination structure with no free solvent, unusual ion transport, improved capacity, and poor PS solubility demonstrate that HCEs can overcome most of the technical limitations associated with dilute electrolytes.

Though HCEs show significant promise in enhancing Li-S battery performance as they reduce PS solubility, the specific impact of the salt anion on these improvements is not fully understood. In this work, we explored the conventional LiTFSI and LiTf along with LiTDI, a relatively new candidate for Li-S battery (Chapter 3). LiTDI-based electrolytes outperform the widely used LiTFSI and LiTf due to their lower PS solubility. This can be attributed to a higher concentration of ion-pairs and aggregates compared to LiTFSI and a less free solvent compared to LiTf. We further explored other Hückel anion-based electrolytes, including LiPDI and LiHDI. The ionic associates based on the local structure and speciation reveal more ion-pairs and aggregates for the long chain Hückel salts, which is reflected in their lower ionic conductivity and higher viscosity. The higher viscosity contributes to lower PS solubility. In contrast, the discharge capacity remained very similar for all three salts. The coulombic efficiency of the Hückel anion-based electrolytes was further improved using the addition of $LiNO_3$ (Chapter 4). The lower PS solubility obtained from our modelling results (Chapter 5) aligns with our *in situ / operando* investigations of these electrolytes in Li-S cells (Chapter 6).

The current work provides a solid foundation for understanding the effect of anion on HCEs. The immediate next step would be transitioning from the Li-S coin cells used herein to larger prototype pouch cells under lean electrolyte conditions for practical applications. Future studies can be done to investigate the Li metal

anode surface and SEI layer stability using concentrated electrolytes and C/S composite cathodes with alternative formulations. A direct comparison of PS formation in Hückel salts versus conventional LiTFSI using *in situ / operando* Raman spectroscopy is yet to be conducted. One of the challenges of using HCEs in this work is their high viscosity. The viscosity can be decreased by the addition of inert solvents or localized highly concentrated electrolytes.

Appendices

A

A.1 *Operando* Raman spectra during first charge-discharge

Operando Raman experiments of the first galvanostatic cycle on (a,b) 1 m LiTDI, LiPDI and LiHDI and (c,d) 2 m LiTDI, LiPDI, LiHDI. (a,c) Raman spectra and (b,d) their corresponding voltage profiles

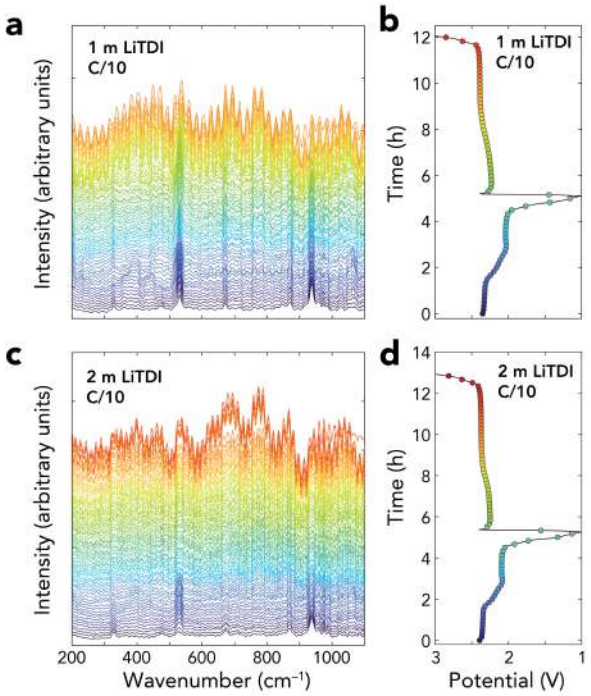

Figure A.1: *Operando* Raman experiments of the first galvanostatic cycle on (a,b) 1 m LiTDI and (c,d) 2 m LiTDI. (a,c) Raman spectra and (b,d) their corresponding voltage profiles

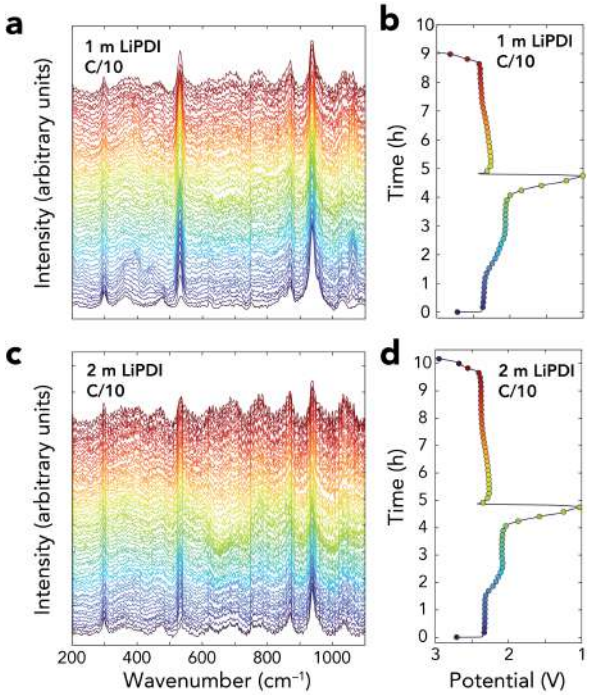

Figure A.2: *Operando* Raman experiments of the first galvanostatic cycle on (a,b) 1 m LiPDI and (c,d) 2 m LiPDI. (a,c) Raman spectra and (b,d) their corresponding voltage profiles.

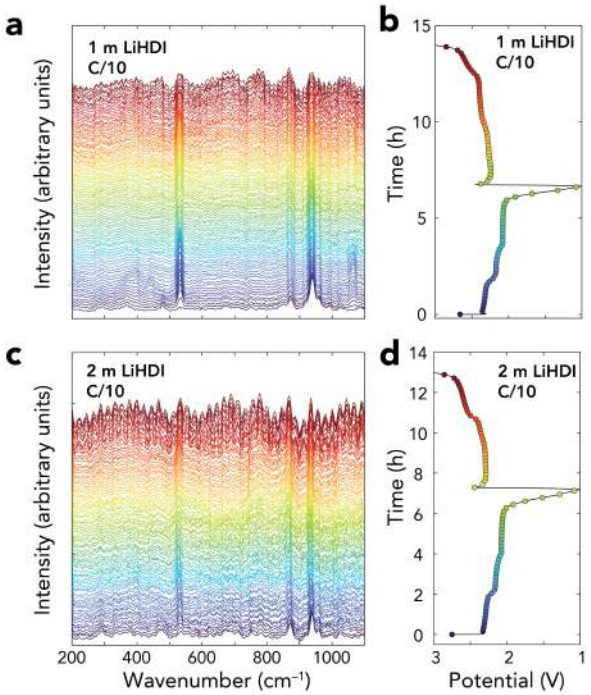

Figure A.3: *Operando* Raman experiments of the first galvanostatic cycle on (a,b) 1 m LiHDI and (c,d) 2 m LiHDI. (a,c) Raman spectra and (b,d) their corresponding voltage profiles

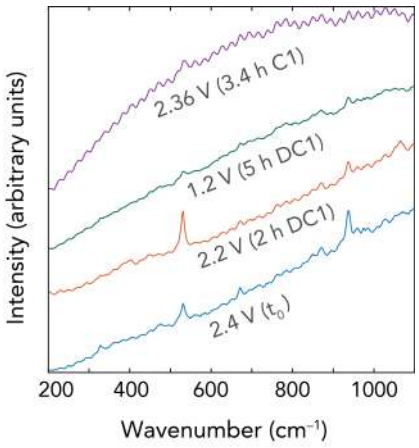

Figure A.4: Raw spectral data of the *operando* Raman experiments on 1 m LiTDI showing the growth of background photoluminescence over the first discharge (DC1) and charge (C1) cycles.

A.2 Deconvolution results and electrolyte properties

Table A.1: The estimated amount of "Free" anions, ion-pairs, aggregates for the LiTFSI, LiTf, and LiTDI in DOL:DME (1:1, v/v) electrolytes after deconvolution.

Bands & systems	**"Free" anions %**	**Ion-pairs %**	**Aggregates %**
δ_s(SNS)	739 cm^{-1}	745 cm^{-1}	747 cm^{-1}
1 m LiTFSI	91	9	
2 m LiTFSI	78	22	
3 m LiTFSI	57	43	
4 m LiTFSI	19	30	51
5 m LiTFSI	13	19	68
6 m LiTFSI	7	45	48
7 m LiTFSI	4	22	74
ν_s(CN)	2227 cm^{-1}	2233 cm^{-1}	2245 cm^{-1}
1 m LiTDI	80	11	8
2 m LiTDI	63	23	14
$\delta_s(CF_3)$	757 cm^{-1}	760 cm^{-1}	763 cm^{-1}
1 m LiTf	74	14	13
2 m LiTf	30	24	46
3 m LiTf	30	19	50
4 m LiTf	16	17	66
5 m LiTf	14	5	81

Table A.2: Solvent to salt mole ratio, viscosity, density at 30°C, and Li_2S_8 solubility using COSMO-RS[112] and the corresponding experimental solubility[23] for LiTFSI (1-7 m), LiTDI (1-2 m), and LiTf (1-5 m) in DOL:DME (1:1, v/v) electrolytes.

Electrolytes	**Mole ratio**	**Viscosity (mPa.s)**	**Density (g cm^{-3})**	**Li_2S_8 solubility**	
				MLR-4 log10[s]	**Exp. log10[s]**
1 m LiTFSI	11.9	1.15	1.12	2.70	2.70
2 m LiTFSI	5.9	2.42	1.22	2.46	-
3 m LiTFSI	3.9	4.35	1.3	2.01	-
5 m LiTFSI	2.4	20.3	1.42	1.62	-
7 m LiTFSI	1.7	225	1.2	1.25	-
1 m LiTDI	11.9	1.08	1.04	1.9	1.92
2 m LiTDI	5.9	2.52	1.1	-	-
1 m LiTf	11.9	0.93	1.07	-	-
2 m LiTf	5.9	1.74	1.14	-	-
3 m LiTf	3.9	3.58	1.19	-	-
5 m LiTf	2.4	16.4	1.28	-	-

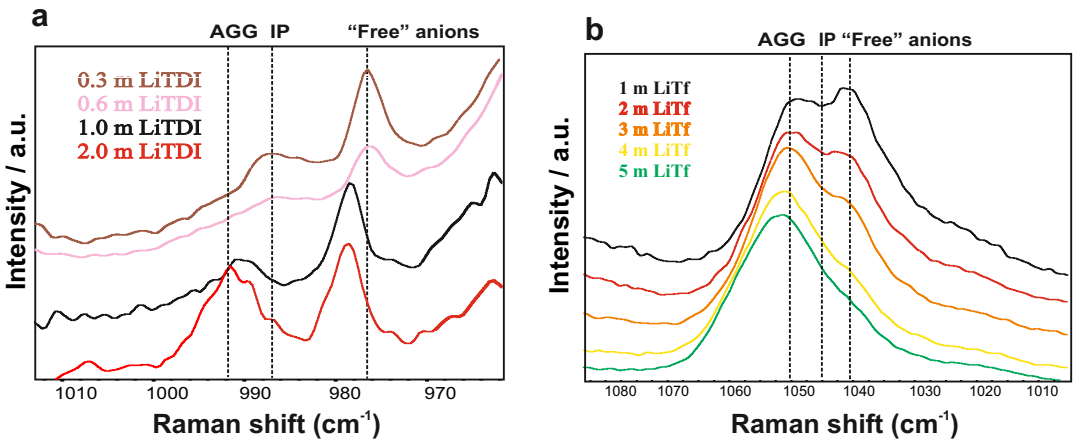

Figure A.5: (a) Raman spectra in the δ_s(N-C-N) bending region for 0.3-2.0 m LiTDI and (b) the $\nu_s(SO_3)$ stretching region for 1-5 m LiTf in DOL:DME (1:1, v/v) electrolytes.

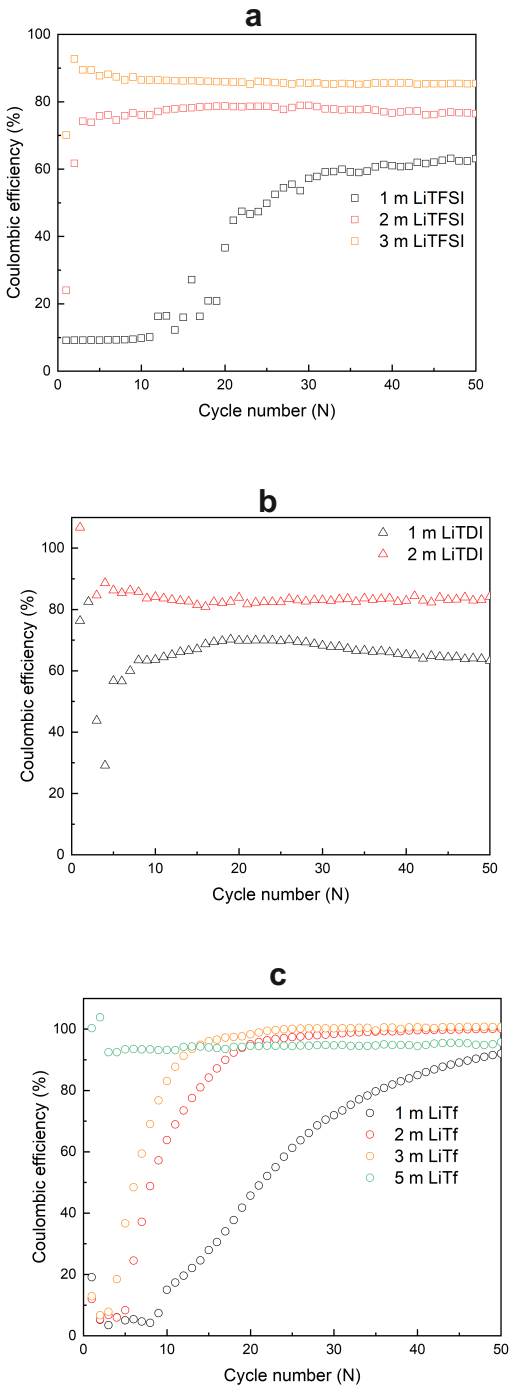

Figure A.6: Comparison of coulombic efficiency of the 1-3 m LiTFSI, 1-2 m LiTDI and 1-5 m LiTf electrolytes with cycle number.

B

B.1 Relation between solubility and chemical potential

The relation between solubility and chemical potential can be derived from the first and second laws of thermodynamics and by combining them with Raoult's law (Physical Chemistry, 3rd Edition, Castellan).

Gibbs free energy for a system is:

$$G = H - TS \tag{B.1}$$

Where:

- G is the Gibbs free energy.
- H is the enthalpy of the system.
- T is the absolute temperature of the system (in Kelvin, K).
- S is the entropy of the system (in joules per Kelvin, J/K).

The enthalpy (H) of a system is given by $H = U + pV$, and Equation B.1 becomes:

$$G = U + PV - TS \tag{B.2}$$

First Law of Thermodynamics: The first law of thermodynamics states that "Energy can neither be created nor destroyed". For a closed system, it can be expressed as:

$$dU = dq + dw \tag{B.3}$$

Where:

- dU is the change in internal energy of the system.
- dq is the heat added to the system.
- dw is the work done by the system.

The differential work done by the system at constant temperature and pressure is given by:

$$dw = -P\,dV \tag{B.4}$$

Equation B.3 becomes:

$$dU = dq - P\,dV \tag{B.5}$$

Second Law of Thermodynamics: The second law of thermodynamics states that for a spontaneous process, the entropy of the universe increases. The differential form of the second law of thermodynamics for a reversible process can be expressed as:

$$dS = \frac{dq_{\text{rev}}}{T} \tag{B.6}$$

Where:

- dS is the differential change in entropy of the system.
- dq_{rev} is the differential heat added to the system in a reversible process.
- T is the temperature of the system in Kelvin.

Combining Equations B.5 and B.6, we get:

$$dU = TdS - PdV \tag{B.7}$$

Taking the total differential of Equation B.2:

$$dG = dU + pdV + Vdp - TdS - SdT \tag{B.8}$$

Combining this with Equation B.7 gives:

$$dG = -SdT + Vdp \tag{B.9}$$

At constant temperature, $dG = Vdp$. Integrating this equation:

$$\int_{p_0}^{p} dG = \int_{p_0}^{p} V\,dp$$

Where:

- dG is the differential change in Gibbs free energy.
- V is the volume.
- p_0 and p are the initial and final pressures, respectively.

Integrating the differential form $dG = V\,dp$ from p_0 to p with $V = \frac{nRT}{p}$ (Ideal gas law) gives:

$$G - G_0 = nRT \ln\left(\frac{p}{p_0}\right) \tag{B.10}$$

Dividing both sides by n gives:

$$\frac{G - G_0}{n} = RT \ln\left(\frac{p}{p_0}\right)$$

Rewriting in terms of chemical potentials μ and μ_0 yields:

$$\mu - \mu_0 = RT \ln \left(\frac{p}{p_0} \right) \tag{B.11}$$

Where:

- μ and μ_0 are the chemical potentials at pressures p and p_0, respectively.
- G and G_0 are the Gibbs free energies at pressures p and p_0, respectively.
- n is the number of moles.
- R is the universal gas constant ($R = 8.314\,\mathrm{J/mol{\cdot}K}$).
- T is the absolute temperature (in Kelvin, K).

For gases, the equation becomes:

$$\mu = \mu_0 + RT \ln p \tag{B.12}$$

Chemical potential and solubility of a solid in a liquid

Consider the equilibrium between a solid and its saturated solution in a liquid. The chemical potential of the solid (μ_{solid}) is equal to the chemical potential of the solute in the liquid phase (μ_{sol}) at equilibrium:

$$\mu_{\text{solid}} = \mu_{\text{sol}} \tag{B.13}$$

For the solute in the liquid phase, the chemical potential is given by:

$$\mu_{\text{sol}} = \mu_{\text{sol}}^0 + RT \ln a_{\text{sol}} \tag{B.14}$$

Where:

- μ_{sol}^0 is the standard chemical potential of the solute in the liquid phase.
- a_{sol} is the activity of the solute in the liquid phase.

At equilibrium, combining this with Equation B.13 gives:

$$\mu_{\text{solid}} = \mu_{\text{sol}}^0 + RT \ln a_{\text{sol}} \tag{B.15}$$

If the solution is ideal, the activity a_{sol} can be approximated by the mole fraction x_{sol} of the solute:

$$a_{\text{sol}} \approx x_{\text{sol}} \tag{B.16}$$

Substituting into Equation B.15:

$$\mu_{\text{solid}} = \mu_{\text{sol}}^0 + RT \ln x_{\text{sol}} \tag{B.17}$$

Solving for x_{sol}, we get the relation between the solubility of the solid (in terms of its mole fraction) and the chemical potentials:

$$x_{\text{sol}} = \exp \left(\frac{\mu_{\text{solid}} - \mu_{\text{sol}}^0}{RT} \right) \tag{B.18}$$

Where:

- x_{sol} is the mole fraction solubility of the solid in the liquid.
- μ_{solid} is the chemical potential of the pure solid.
- μ^0_{sol} is the standard chemical potential of the solute in the liquid phase.
- R is the universal gas constant ($R = 8.314\,\text{J/mol·K}$).
- T is the absolute temperature (in Kelvin, K).

Equation B.18 gives the relationship between the chemical potential and the solubility of a solid in a liquid mixture.

Bibliography

1. Chen, Y. *et al.* Advances in lithium–sulfur batteries: from academic research to commercial viability. *Advanced Materials* **33,** 2003666 (2021).
2. Zhang, X. *et al.* Advances in lithium—sulfur batteries. *Materials Science and Engineering: R: Reports* **121,** 1–29 (2017).
3. Mikhaylik, Y. V. *et al.* High energy rechargeable Li-S cells for EV application: status, remaining problems and solutions. *Ecs Transactions* **25,** 23 (2010).
4. Tian, Y. *et al.* Promises and challenges of next-generation "beyond Li-ion" batteries for electric vehicles and grid decarbonization. *Chemical reviews* **121,** 1623–1669 (2020).
5. Fazel, M. & Mehrdad, S. A comprehensive overview of electric vehicle batteries market. *e-Prime-Advances in Electrical Engineering, Electronics and Energy* **3** (2023).
6. Benveniste, G., Sánchez, A., Rallo, H., Corchero, C. & Amante, B. Comparative life cycle assessment of Li-Sulphur and Li-ion batteries for electric vehicles. *Resources, Conservation & Recycling Advances* **15,** 200086 (2022).
7. International Energy Agency. *Global EV Outlook 2024* Licence: CC BY 4.0 (International Energy Agency, Paris, 2024). `https://www.iea.org/reports/global-ev-outlook-2024`.
8. Etxandi-Santolaya, M., Casals, L. C., Montes, T. & Corchero, C. Are electric vehicle batteries being underused? A review of current practices and sources of circularity. *Journal of environmental management* **338,** 117814 (2023).
9. Wu, F., Maier, J. & Yu, Y. Guidelines and trends for next-generation rechargeable lithium and lithium-ion batteries. *Chemical Society Reviews* **49,** 1569–1614 (2020).
10. Linden, D. *Handbook of batteries* in *Fuel and energy abstracts* **4** (1995), 265.
11. Danuta, H. & Juliusz, U. 3,043,896 (1962).
12. Ji, X., Lee, K. T. & Nazar, L. F. A highly ordered nanostructured carbon–sulphur cathode for lithium–sulphur batteries. *Nature materials* **8,** 500–506 (2009).
13. Johansson, P. & Dominko, R. *EUROLIS—European lithium sulphur cells for automotive applications* in *2013 World Electric Vehicle Symposium and Exhibition (EVS27)* (2013), 1–3.

14. *LIS Technology Gets Ready for Space Missions* Accessed: 2024-05-29. 2024. `https://cordis.europa.eu/article/id/231213-lis-technology-gets-ready-for-space-missions`.
15. *Li-S Energy gets super charged up for 2023* Accessed: 2024-05-29. 2023. `https://stockhead.com.au/tech/li-s-energy-gets-super-charged-up-for-2023/`.
16. Kim, H.-S. *et al.* Boron nitride nanotube-based separator for high-performance lithium-sulfur batteries. *Nanomaterials* **12,** 11 (2021).
17. Scheers, J., Fantini, S. & Johansson, P. A review of electrolytes for lithium–sulphur batteries. *Journal of Power sources* **255,** 204–218 (2014).
18. Xu, K. Nonaqueous liquid electrolytes for lithium-based rechargeable batteries. *Chemical reviews* **104,** 4303–4418 (2004).
19. Arote, S. A. *Lithium-ion and Lithium–Sulfur Batteries: Fundamentals to performance* (IOP Publishing, 2022).
20. Chung, S.-H. & Manthiram, A. Designing lithium-sulfur cells with practically necessary parameters. *Joule* **2,** 710–724 (2018).
21. Lv, D. *et al.* High energy density lithium–sulfur batteries: challenges of thick sulfur cathodes. *Advanced Energy Materials* **5,** 1402290 (2015).
22. Xiao, J. Understanding the Lithium Sulfur Battery System at Relevant Scales. *Advanced Energy Materials* **5** (2015).
23. Chen, J. *et al.* Restricting the Solubility of Polysulfides in Li-S Batteries Via Electrolyte Salt Selection. *Adv. Energy Mater.* **6,** 1600160 (2016).
24. Liu, Y.-K. *et al.* Research Progresses of Liquid Electrolytes in Lithium-Ion Batteries. *Small* **19,** 2205315 (2023).
25. Barghamadi, M. *et al.* Lithium–sulfur batteries—the solution is in the electrolyte, but is the electrolyte a solution? *Energy Environ Sci.* **7,** 3902 (2014).
26. Gofer, Y., Ely, Y. E. & Aurbach, D. Surface chemistry of lithium in 1, 3-dioxolane. *Electrochimica acta* **37,** 1897–1899 (1992).
27. Adams, B. D. *et al.* Long term stability of Li-S batteries using high concentration lithium nitrate electrolytes. *Nano Energy* **40,** 607 (2017).
28. Mikhaylik, Y. V. U.S. Patent No. 7358012 (2008).
29. Liang, X. *et al.* Improved cycling performances of lithium sulfur batteries with LiNO3-modified electrolyte. *Journal of Power Sources* **196,** 9839–9843 (2011).
30. Aurbach, D. *et al.* On the surface chemical aspects of very high energy density, rechargeable Li–sulfur batteries. *Journal of The Electrochemical Society* **156,** A694 (2009).
31. Yin, Y.-X., Xin, S., Guo, Y.-G. & Wan, L.-J. Lithium–sulfur batteries: electrochemistry, materials, and prospects. *Angewandte Chemie International Edition* **52,** 13186–13200 (2013).

32. Tarascon, J.-M. & Armand, M. Issues and challenges facing rechargeable lithium batteries. *nature* **414,** 359–367 (2001).

33. Song, M.-K., Cairns, E. J. & Zhang, Y. Lithium/sulfur batteries with high specific energy: old challenges and new opportunities. *Nanoscale* **5,** 2186–2204 (2013).

34. Zheng, G., Yang, Y., Cha, J. J., Hong, S. S. & Cui, Y. Hollow carbon nanofiber-encapsulated sulfur cathodes for high specific capacity rechargeable lithium batteries. *Nano letters* **11,** 4462–4467 (2011).

35. Hagen, M. *et al.* Lithium–sulfur cells: the gap between the state-of-the-art and the requirements for high energy battery cells. *Advanced Energy Materials* **5,** 1401986 (2015).

36. Ma, L. *et al.* Cerium oxide nanocrystal embedded bimodal micromesoporous nitrogen-rich carbon nanospheres as effective sulfur host for lithium–sulfur batteries. *ACS nano* **11,** 7274–7283 (2017).

37. Wang, F. *et al.* Nanostructured positive electrode materials for post-lithium ion batteries. *Energy & Environmental Science* **9,** 3570–3611 (2016).

38. Mikhaylik, Y. V. & Akridge, J. R. Polysulfide shuttle study in the Li/S battery system. *J. Electrochem. Soc.* **151,** A1969 (2004).

39. Yamada, Y. & Yamada, A. Superconcentrated electrolytes for lithium batteries. *J. Electrochem. Soc.* **162,** A2406 (2015).

40. McKinnon, W. & Dahn, J. How to reduce the cointercalation of propylene carbonate in Li x ZrS2 and other layered compounds. *Journal of The Electrochemical Society* **132,** 364 (1985).

41. Suo, L. *et al.* "Water-in-salt" electrolyte makes aqueous sodium-ion battery safe, green, and long-lasting. *Advanced Energy Materials* **7,** 1701189 (2017).

42. Wang, F. *et al.* High-voltage aqueous magnesium ion batteries. *ACS central science* **3,** 1121–1128 (2017).

43. Lee, C. & Jeong, S.-K. A novel superconcentrated aqueous electrolyte to improve the electrochemical performance of calcium-ion batteries. *Chemistry Letters* **45,** 1447–1449 (2016).

44. Leonard, D. P., Wei, Z., Chen, G., Du, F. & Ji, X. Water-in-salt electrolyte for potassium-ion batteries. *ACS Energy Letters* **3,** 373–374 (2018).

45. Dokko, K. *et al.* Solvate ionic liquid electrolyte for Li–S batteries. *J. Electrochem. Soc.* **160,** A1304 (2013).

46. Chen, S. *et al.* High-voltage lithium-metal batteries enabled by localized high-concentration electrolytes. *Advanced materials* **30,** 1706102 (2018).

47. Zheng, J. *et al.* Extremely stable sodium metal batteries enabled by localized high-concentration electrolytes. *ACS Energy Letters* **3,** 315–321 (2018).

48. Shin, E. S., Kim, K., Oh, S. H. & Cho, W. I. Polysulfide dissolution control: the common ion effect. *Chem. Commun.* **49,** 2004 (2013).

49. Henderson, W. A. *et al.* Electrolyte solvation and ionic association: VIII. Reassessing Raman spectroscopic studies of ion coordination for LiTFSI. *Journal of The Electrochemical Society* **169,** 060515 (2022).
50. Alia, J. M. & Edwards, H. G. Ion solvation and ion association in lithium trifluoromethanesulfonate solutions in three aprotic solvents. An FT-Raman spectroscopic study. *Vibrational Spectroscopy* **24,** 185–200 (2000).
51. Brouillette, D. *et al.* Stable solvates in solution of lithium bis (trifluoromethylsulfone) imide in glymes and other aprotic solvents: Phase diagrams, crystallography and Raman spectroscopy. *Physical Chemistry Chemical Physics* **4,** 6063–6071 (2002).
52. Kreuer, K.-D., Rabenau, A. & Weppner, W. Vehicle mechanism, a new model for the interpretation of the conductivity of fast proton conductors. *Angewandte Chemie International Edition in English* **21,** 208–209 (1982).
53. Forsyth, M. *et al.* Novel Na+ Ion Diffusion Mechanism in Mixed Organic–Inorganic Ionic Liquid Electrolyte Leading to High Na+ Transference Number and Stable, High Rate Electrochemical Cycling of Sodium Cells. *The Journal of Physical Chemistry C* **120,** 4276–4286 (2016).
54. Tsurumura, T., Hashimoto, Y., Morita, M., Umebayashi, Y. & Fujii, K. Anion Coordination Characteristics of Ion-pair Complexes in Highly Concentrated Aqueous Lithium Bis (trifluoromethane-sulfonyl) amide Electrolytes. *Anal. Sci.* **35,** 289 (2019).
55. Han, S.-D., Borodin, O., Seo, D. M., Zhou, Z.-B. & Henderson, W. A. Electrolyte solvation and ionic association: V. Acetonitrile-lithium bis (fluorosulfonyl) imide (LiFSI) mixtures. *Journal of The Electrochemical Society* **161,** A2042 (2014).
56. Suo, L., Hu, Y.-S., Li, H., Armand, M. & Chen, L. A new class of solvent-in-salt electrolyte for high-energy rechargeable metallic lithium batteries. *Nat. Commun.* **4,** 1481 (2013).
57. Niedzicki, L. *et al.* New type of imidazole based salts designed specifically for lithium ion batteries. *Electrochim. Acta* **55,** 1450 (2010).
58. Paar, A. Instruction Manual DMA 4100 M DMA 4500 M DMA 5000 M Firmware Version: V2. 21. *Graz, Austria* (2012).
59. Abu Deham, Y. *Investigating Polymer Degradation in Medical Device Production Using Inherent Viscosity Measurements* (2023).
60. Pryde, S. & Gilbert, M. T. *Applications of high performance liquid chromatography* (Springer Science & Business Media, 1979).
61. Zheng, D. *et al.* Quantitative chromatographic determination of dissolved elemental sulfur in the non-aqueous electrolyte for lithium-sulfur batteries. *J. Electrochem. Soc.* **162,** A203 (2014).
62. Stuart, B. *Infrared Spectroscopy: Fundamentals and Applications* HB; 0-470-85428-6 (PB). ISBN: 0-470-85427-8 (John Wiley & Sons, Ltd, 2004).

63. Larkin, P. *Infrared and Raman spectroscopy: principles and spectral interpretation* (Elsevier, 2017).

64. Frech, R., Chintapalli, S., Bruce, P. G. & Vincent, C. A. Crystalline and amorphous phases in the poly (ethylene oxide)- LiCF3SO3 system. *Macromolecules* **32,** 808–813 (1999).

65. Jankowski, P., Dranka, M., Zukowska, G. Z. & Zachara, J. Structural studies of lithium 4, 5-dicyanoimidazolate–glyme solvates. 1. From isolated free ions to conductive aggregated systems. *J. Phys. Chem. C* **119,** 9108 (2015).

66. Christian, G. D. *Analytical Chemistry* 6th ed. ISBN: 0471214728; 9780471214724 (Wiley, 2003).

67. Torell, L., Schantz, S. & Jacobson, P. Raman Study of Free Volume Effects on Ion Pairs in Polymer Electrolytes. *MRS Online Proceedings Library (OPL)* **210,** 221 (1990).

68. Hannauer, J. *et al.* The quest for polysulfides in lithium–sulfur battery electrolytes: an operando confocal Raman spectroscopy study. *ChemPhysChem* **16,** 2755–2759 (2015).

69. Hagen, M. *et al.* In-situ Raman investigation of polysulfide formation in Li-S cells. *Journal of The Electrochemical Society* **160,** A1205 (2013).

70. Sadd, M. J. *Operando Analysis of Materials and Processes in Next Generation Batteries* PhD thesis (Chalmers Tekniska Hogskola (Sweden), 2021).

71. EC-Lab®/BT-Lab®. *EC-Lab®/BT-Lab® Software User's Manual* Software User's Manual (June 2021).

72. Magar, H. S., Hassan, R. Y. & Mulchandani, A. Electrochemical impedance spectroscopy (EIS): Principles, construction, and biosensing applications. *Sensors* **21,** 6578 (2021).

73. Lazanas, A. C. & Prodromidis, M. I. Electrochemical impedance spectroscopy a tutorial. *ACS Measurement Science Au* **3,** 162–193 (2023).

74. Hannan, M. A. *et al.* Toward enhanced state of charge estimation of lithium-ion batteries using optimized machine learning techniques. *Scientific reports* **10,** 4687 (2020).

75. Castelli, I. E. *et al.* Data Management Plans: the Importance of Data Management in the BIG-MAP Project. *Batteries & Supercaps* **4,** 1803–1812 (2021).

76. Morgan, L. M. *et al.* From Atoms to Cells: Multiscale Modeling of LiNi x Mn y Co z O2 Cathodes for Li-Ion Batteries. *ACS Energy Letters* **7,** 108–122 (2021).

77. Amici, J. *et al.* A roadmap for transforming research to invent the batteries of the future designed within the european large scale research initiative battery 2030+. *Advanced energy materials* **12,** 2102785 (2022).

78. Klamt, A., Jonas, V., Bürger, T. & Lohrenz, J. C. Refinement and parametrization of COSMO-RS. *J. Phys. Chem. A* **102,** 5074 (1998).

79. Klamt, A. The COSMO and COSMO-RS solvation models. *Wiley Interdiscip. Rev. Comput. Mol. Sci.* **1,** 699 (2011).

80. Klamt, A. & Schüürmann, G. COSMO: a new approach to dielectric screening in solvents with explicit expressions for the screening energy and its gradient. *Journal of the Chemical Society, Perkin Transactions 2,* 799–805 (1993).

81. Klamt, A. Conductor-like screening model for real solvents: a new approach to the quantitative calculation of solvation phenomena. *The Journal of Physical Chemistry* **99,** 2224–2235 (1995).

82. Klamt, A. & Eckert, F. COSMO-RS: a novel and efficient method for the a priori prediction of thermophysical data of liquids. *Fluid Phase Equilibria* **172,** 43–72 (2000).

83. Jeschke, S. & Johansson, P. Predicting the Solubility of Sulfur: A COSMO-RS-Based Approach to Investigate Electrolytes for Li–S Batteries. *Chem. - Eur. J.* **23,** 9130 (2017).

84. *TURBOMOLE V7.7 2022, a development of University of Karlsruhe and Forschungszentrum Karlsruhe GmbH, 1989-2007, TURBOMOLE GmbH, since 2007; available from* `https://www.turbomole.org`.

85. Perdew, J. P. Density-functional approximation for the correlation energy of the inhomogeneous electron gas. *Phys. Rev. B.* **33,** 8822 (1986).

86. Becke, A. D. Density-functional exchange-energy approximation with correct asymptotic behavior. *Phys. Rev. A.* **38,** 3098 (1988).

87. Angell, C., Liu, C. & Sanchez, E. Rubbery solid electrolytes with dominant cationic transport and high ambient conductivity. *Nature* **362,** 137 (1993).

88. Ferry, A., Edman, L., Forsyth, M., MacFarlane, D. R. & Sun, J. Connectivity, ionic interactions, and migration in a fast-ion-conducting polymer-in-salt electrolyte based on poly (acrylonitrile) and LiCF 3 SO 3. *J. Appl. Phys.* **86,** 2346 (1999).

89. Nakanishi, A. *et al.* Sulfolane-based highly concentrated electrolytes of lithium bis (trifluoromethanesulfonyl) amide: ionic transport, Li-Ion coordination, and Li–S battery performance. *J. Phys. Chem. C* **123,** 14229 (2019).

90. Jiang, G. *et al.* Perspective on high-concentration electrolytes for lithium metal batteries. *Small Structures* **2,** 2000122 (2021).

91. Zhang, S., Ueno, K., Dokko, K. & Watanabe, M. Recent advances in electrolytes for lithium–sulfur batteries. *Adv. Energy Mater.* **5,** 1500117 (2015).

92. Cheng, L. *et al.* Sparingly solvating electrolytes for high energy density lithium–sulfur batteries. *ACS Energy Lett.* **1,** 503 (2016).

93. Yamada, Y. *et al.* Unusual stability of acetonitrile-based superconcentrated electrolytes for fast-charging lithium-ion batteries. *J. Am. Chem. Soc.* **136,** 5039 (2014).

94. Lin, Y. *et al.* Organic liquid electrolytes in Li-S batteries: actualities and perspectives. *Energy Storage Mater.* **34,** 128 (2021).

95. Park, J.-W., Ueno, K., Tachikawa, N., Dokko, K. & Watanabe, M. Ionic liquid electrolytes for lithium–sulfur batteries. *J. Phys. Chem. C* **117,** 20531 (2013).

96. Han, K. S. *et al.* Effects of anion mobility on electrochemical behaviors of lithium–sulfur batteries. *Chem. Mater.* **29,** 9023 (2017).

97. Yamada, Y., Wang, J., Ko, S., Watanabe, E. & Yamada, A. Advances and issues in developing salt-concentrated battery electrolytes. *Nat. Energy* **4,** 269 (2019).

98. Han, S.-D. *et al.* Electrolyte solvation and ionic association: IV. Acetonitrile-lithium difluoro (oxalato) borate (LiDFOB) mixtures. *J. Electrochem. Soc.* **160,** A2100 (2013).

99. Seo, D. M. *et al.* Electrolyte solvation and ionic association. *J. Electrochem. Soc.* **159,** A553 (2012).

100. Huang, W., Frech, R. & Wheeler, R. A. Molecular structures and normal vibrations of trifluoromethane sulfonate (CF3SO3-) and its lithium ion pairs and aggregates. *J. Phys. Chem.* **98,** 100 (1994).

101. Scheers, J. *et al.* Ion–ion and ion–solvent interactions in lithium imidazolide electrolytes studied by Raman spectroscopy and DFT models. *Phys. Chem. Chem. Phys.* **13,** 11136 (2011).

102. Suo, L., Zheng, F., Hu, Y.-S. & Chen, L. FT-Raman spectroscopy study of solvent-in-salt electrolytes. *Chin. Phys. B.* **25,** 016101 (2015).

103. Henderson, W. A. Glyme- lithium salt phase behavior. *J. Phys. Chem. B* **110,** 13177 (2006).

104. McOwen, D. W. *et al.* Anion coordination interactions in solvates with the lithium salts LiDCTA and LiTDI. *J. Phys. Chem. C* **118,** 7781 (2014).

105. Jow, T. R., Xu, K., Borodin, O. & Ue, M. *Electrolytes for lithium and lithium-ion batteries* (Springer, 2014).

106. Schreiner, C., Zugmann, S., Hartl, R. & Gores, H. J. Fractional Walden rule for ionic liquids: examples from recent measurements and a critique of the so-called ideal KCl line for the Walden plot. *J. Chem. Eng. Data.* **55,** 1784 (2010).

107. Lundin, F. *et al.* Structure and dynamics of highly concentrated LiTFSI/acetonitrile electrolytes. *Physical Chemistry Chemical Physics* **23,** 13819–13826 (2021).

108. Seo, D. M. *et al.* Electrolyte solvation and ionic association III. Acetonitrile-lithium salt mixtures–transport properties. *J. Electrochem. Soc.* **160,** A1061 (2013).

109. Callsen, M., Sodeyama, K., Futera, Z., Tateyama, Y. & Hamada, I. The solvation structure of lithium ions in an ether based electrolyte solution from first-principles molecular dynamics. *The Journal of Physical Chemistry B* **121,** 180–188 (2017).

110. Dokko, K. *et al.* Direct evidence for Li ion hopping conduction in highly concentrated sulfolane-based liquid electrolytes. *J. Phys. Chem. B* **122,** 10736 (2018).

111. Ueno, K. *et al.* Anionic effects on solvate ionic liquid electrolytes in rechargeable lithium–sulfur batteries. *J. Phys. Chem. C* **117,** 20509 (2013).

112. Jeschke, S. & Johansson, P. Supervised Machine Learning-Based Classification of Li- S Battery Electrolytes. *Batteries & Supercaps* **4,** 1156–1162 (2021).

113. Pan, H. *et al.* On the way toward understanding solution chemistry of lithium polysulfides for high energy Li–S redox flow batteries. *Advanced Energy Materials* **5,** 1500113 (2015).

114. Armand, M. *et al.* development of Hückel type anions: from molecular modeling to industrial commercialization. A success story. *Journal of The Electrochemical Society* **167,** 070562 (2020).

115. Niedzicki, L. *et al.* Optimization of the lithium-ion cell electrolyte composition through the use of the LiTDI salt. *Electrochim. Acta* **117,** 224 (2014).

116. Szczęsna-Chrzan, A. *et al.* Ionic conductivity, viscosity, and self-diffusion coefficients of novel imidazole salts for lithium-ion battery electrolytes. *Journal of Materials Chemistry A* **11,** 13483–13492 (2023).

117. Niedzicki, L. *et al.* Liquid electrolytes based on new lithium conductive imidazole salts. *Journal of Power Sources* **196,** 1386–1391 (2011).

118. Ueno, K. *et al.* Li+ solvation in glyme–Li salt solvate ionic liquids. *Physical Chemistry Chemical Physics* **17,** 8248–8257 (2015).

119. Grondin, J. *et al.* Raman study of tetraglyme–LiClO4 solvate structures. *Physical Chemistry Chemical Physics* **6,** 4260–4267 (2004).

120. Ducasse, L. *et al.* Spectroscopic study of poly (ethylene oxide) 6: LiX complexes (X= PF 6, AsF 6, SbF 6, ClO 4). *Physical Chemistry Chemical Physics* **5,** 567–574 (2003).

121. Broszkiewicz, M., Zalewska, A. & Niedzicki, L. Comparison of LiTDI and LiPDI salts and influence of their perfluoroalkyl side-chain on association and electrochemical properties in triglyme. *Ionics* **25,** 3651–3660 (2019).

122. Saqib, N., Silva, C. J., Maupin, C. M. & Porter, J. M. A novel optical diagnostic for in situ measurements of lithium polysulfides in battery electrolytes. *Applied Spectroscopy* **71,** 1593–1599 (2017).

123. Barchasz, C. *et al.* Lithium/sulfur cell discharge mechanism: an original approach for intermediate species identification. *Analytical chemistry* **84,** 3973–3980 (2012).

124. Pang, Q. *et al.* Tuning the electrolyte network structure to invoke quasi-solid state sulfur conversion and suppress lithium dendrite formation in Li–S batteries. *Nature Energy* **3,** 783–791 (2018).

125. Zhang, C. *et al.* Chelate effects in glyme/lithium bis (trifluoromethanesulfonyl) amide solvate ionic liquids. I. Stability of solvate cations and correlation with electrolyte properties. *The Journal of Physical Chemistry B* **118,** 5144–5153 (2014).

126. Park, J.-W. *et al.* Solvent effect of room temperature ionic liquids on electrochemical reactions in lithium–sulfur batteries. *The Journal of Physical Chemistry C* **117,** 4431–4440 (2013).

127. Zhang, C. *et al.* Chelate effects in glyme/lithium bis (trifluoromethanesulfonyl) amide solvate ionic liquids, part 2: Importance of solvate-structure stability for electrolytes of lithium batteries. *The Journal of Physical Chemistry C* **118,** 17362–17373 (2014).

128. Jeschke, S. & Cole, I. S. 3D-QSAR for binding constants of β-cyclodextrin host-guest complexes by utilising spectrophores as molecular descriptors. *Chemosphere* **225,** 135–138 (2019).

129. Bouchal, R., Boulaoued, A. & Johansson, P. Monitoring polysulfide solubility and diffusion in fluorinated ether-based electrolytes by operando Raman spectroscopy. *Batteries & Supercaps* **3,** 397–401 (2020).